Stability theory for metal pad roll in cylindrical liquid metal batteries

Herreman, W.; Wierzchalek, L.; Horstmann, G. M.; Cappanera, L.; Nore, C.;

Originally published:

April 2023

Journal of Fluid Mechanics 962(2023)A6

DOI: https://doi.org/10.1017/jfm.2023.238

Stability theory for metal pad roll in cylindrical liquid metal batteries

Journal:	*Journal of Fluid Mechanics*
Manuscript ID	Draft
Manuscript Type:	JFM Papers
Date Submitted by the Author:	n/a
Complete List of Authors:	Herreman, Wietze; LIMSI, CNRS, Université Paris-Sud, Université Paris-Saclay, Mechanics Wierzchalek, Ladislas; LIMSI, CNRS, Université Paris-Sud, Université Paris-Saclay, Mechanics Horstmann, Gerrit; Helmholtz-Zentrum Dresden - Rossendorf e.V., Institute of Fluid Dynamics Cappanera, Loïc; Rice University, Department of Computational and Applied Mathematics Nore, Caroline; LIMSI, CNRS UPR 3251,
JFM Keywords:	MHD and Electrohydrodynamics, Waves/Free-surface Flows
Abstract:	We theoretically calculate the growth rate of the metal pad roll instability in cylindrically shaped liquid metal batteries. Our model extends that of Herreman et al. (2019) and includes a precise description of dissipation. Theoretical growth rates are in quantitive agreement with the simulations of Weber et al. (2017b) and Horstmann et al. (2018). Our model suggests that the metal pad roll instability in batteries has a distinct feature: the Lorentz force can be destabilizing in one fluid layer and stabilizing in another and this may result in a very weak instability. The existence of such a weak instability region explains why different types of waves can be selected as most unstable modes. We use our theory to estimate the domain of stability of different types of large scale, shallow liquid metal batteries.

Under consideration for publication in J. Fluid Mech.

Stability theory for metal pad roll in cylindrical liquid metal batteries

W. Herreman†[1], L. Wierzchalek[1], G. M. Horstmann [2], L. Cappanera [3] and C. Nore[1]

[1]Université Paris-Saclay, CNRS, LISN, 91400 Orsay, France

[2]Helmholtz-Zentrum Dresden-Rossendorf, Germany

[3]Department of Mathematics, University of Houston, Houston, TX 77204-3008, USA

(Received xx; revised xx; accepted xx)

We theoretically calculate the growth rate of the metal pad roll instability in cylindrically shaped liquid metal batteries. Our model extends that of Herreman *et al.* (2019) and includes a precise description of dissipation. Theoretical growth rates are in quantitive agreement with the simulations of Weber *et al.* (2017*b*) and Horstmann *et al.* (2018). Our model suggests that the metal pad roll instability in batteries has a distinct feature: the Lorentz force can be destabilizing in one fluid layer and stabilizing in another and this may result in a very weak instability. The existence of such a weak instability region explains why different types of waves can be selected as most unstable modes. We use our theory to estimate the domain of stability of different types of large scale, shallow liquid metal batteries.

Key words: Magnetohydrodynamics (MHD), gravity waves

---

1. Introduction

The metal pad roll instability is a well known phenomenon that causes undesirable wave motion on the cryolite-aluminium interface inside Hall-Héroult reduction cells. Since Sele (1977), we know that this wave motion is due to a weak magnetohydrodynamic coupling between the ambient magnetic field and the electrolysis current that is being deflected by the waves. The review of Gerbeau *et al.* (2006) contains a rich bibliography on this subject.

Liquid metal batteries are structurally similar to reduction cells but have three layers of stacked fluids (light metal, molten salt, heavy alloy) rather than two (cryolite, aluminium). Existing prototypes of liquid metal batteries (Bradwell *et al.* 2012; Wang *et al.* 2014) are certainly not yet as large as industrial reduction cells, but if they would be made as large in the future, then it is certain that metal pad roll instability would also be present in these batteries and affect their efficiency. The first article to discuss metal pad roll instability inside liquid metal batteries is Zikanov (2015), who extends the solid-slab model of Davidson & Lindsay (1998) to the three layer case. This suggested that the physical mechanism

† Email address for correspondence: wietze.herreman@universite-paris-saclay.fr

causing metal pad instability in batteries is essentially the same one as in reduction cells. Shallow, magnetohydrodynamical models give a more precise description of the metal pad roll instability and were very popular in reduction cell context (see Bojarevics & Romerio (1994); Bojarevics (1998); Davidson & Lindsay (1998); Zikanov *et al.* (2000); Lukyanov *et al.* (2001); Sun *et al.* (2004); Zikanov *et al.* (2004)). This shallow approach has inspired Bojarevics & Tucs (2017); Tucs *et al.* (2018*a*,*b*); Molokov (2018) to propose three layer extensions, adapted to batteries. All these models suggest that the type of waveform that is most unstable will depend on the type of battery, the materials and also the geometry of the cell. As shown by Tucs *et al.* (2018*b*), we can use these shallow models to estimate stability thresholds of future, large scale, shallow liquid metal batteries.

In parallel to the shallow approach, several groups have done direct numerical simulations (DNS) of metal pad roll instability in *much smaller* liquid metal batteries that are *non-shallow* (Weber *et al.* 2017*b*,*a*; Horstmann *et al.* 2018; Xiang & Zikanov 2019). This alternative numerical approach relies on much less assumptions but is computationally much more demanding. Unlike in the shallow approach, small scale motion is not filtered out and hence it needs to be resolved. In practice, this means that, without turbulence model, DNS is limited to moderate Reynolds number flows $Re < 10^4$, in order to have a not too turbulent flow. With realistic viscosities that are of order $10^{-6}\,\mathrm{m}^2\,\mathrm{s}^{-1}$ or lower, a typical flow of just $1\ \mathrm{cm\ s}^{-2}$, we already reach this typical DNS limit of $Re \approx 10^4$ in small, centimeter scale cells. This explains why all DNS of metal pad roll instability inside liquid metal batteries have been done in small, centimeter scale cells. In such small batteries, instability requires much larger ambient magnetic field or electrical currents and viscous and magnetic dissipation are not negligible. In Weber *et al.* (2017*b*,*a*), metal pad roll instability is reproduced numerically in a small Mg||Sb liquid metal battery. Many physical parameters (current, imposed magnetic field, viscosities, densities, fluid layer heights, ...) were varied to show how these parameters affect the instability. Horstmann *et al.* (2018) continued this work in a more fundamental study. It is shown that the ratio of the density jumps $(\rho_3 - \rho_2)/(\rho_2 - \rho_1)$ is an important parameter in selecting the most unstable wave-mode. If this number is close to 1, then both interfaces will move with similar amplitudes and hydrodynamically, they are strongly coupled. When on the contrary, the ratio is very different from 1, the interfaces are decoupled and the most unstable wave will mainly deform the interface with the lowest density jump. Next to the metal pad roll instability, it is also shown that a non-oscillatory, axisymmetric bulge instability can also appear though transiently. Finally, Xiang & Zikanov (2019) have also done a numerical study on metal pad roll in cubical cells. Different types of wave motion are again observed and the importance of the parameter $(\rho_3-\rho_2)/(\rho_2-\rho_1)$ in selecting these different modes is acknowledged. All combined, DNS have provided valuable information on the metal pad roll instability, but a deeper theoretical understanding of what is going on inside these smaller cells is certainly desirable. The problem is that none of the existing shallow stability models are really adapted to describe instability in these small and non-shallow cells.

The absence of theoretical stability models for small cells, that hence can be compared with DNS, is precisely what motivated Herreman *et al.* (2019) (referred to as H19 hereafter) to derive a new type of stability model. Rather than using a shallow approximation, a perturbative expansion on gravity waves is done to calculate the small growth rate of rotating gravity waves. Using solvability conditions, it is possible to calculate how rotating gravity waves are slightly destabilized by the Lorentz force (Sele-mechanism) and how they are slightly stabilized by viscosity. The stability theory of H19 is presently limited to cylindrical cells with two fluid layers and results in explicit formula for the growth rates. For the small cylindrical reduction cell studied by Steiner (2009), it was shown that these theoretical growth rates are in quantitative agreement with measurements from DNS. The theoretical

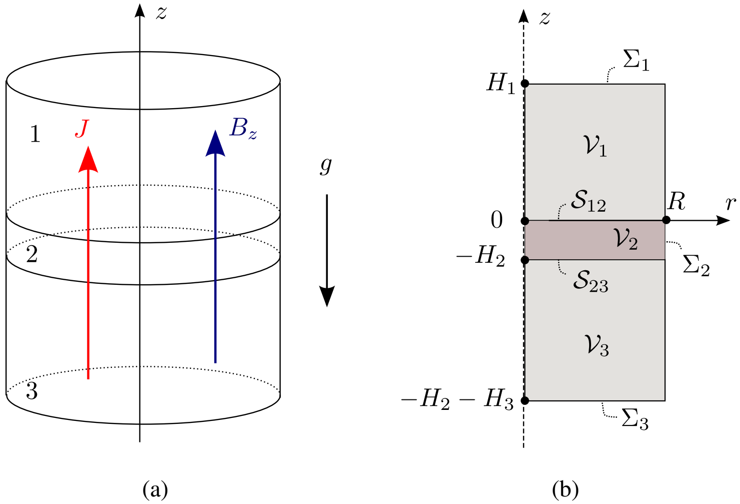

Figure 1: Sketch of the base state under study. (a) Three liquid layers with different electrical conductivity, density and kinematic viscosity are stably stacked on top of each other due to gravity. A homogenous current density J runs vertically through the layers and there is an ambient and uniform vertical magnetic field B_z. (b) Our three fluid domains $\mathcal{V}_1, \mathcal{V}_2, \mathcal{V}_3$ have respective heights H_1, H_2, H_3 and radius R. The solid boundaries are referred to as $\Sigma_1, \Sigma_2, \Sigma_3$ and the interfaces as $\mathcal{S}_{12}$ and $\mathcal{S}_{23}$.

expressions for the viscous damping rates of the waves were independently validated in dedicated hydrodynamical experiments (Horstmann & Wylega 2019). All this suggest that this new type of stability theory has predictive power. In Nore *et al.* (2021), we have used this theory to advocate why metal pad roll instability should be realizable in a small room-temperature experimental set-up that places a layer of gallium above a layer of mercury. Such an experiment would be interesting as there are very few devices that can reproduce this instability in the lab (Pedchenko *et al.* 2009, 2016). Nore *et al.* (2021) also found excellent agreement between theory and DNS and we must note that these simulations are amongst the most challenging ones that have been ever done on the metal pad roll instability.

In this article we continue our program on the theoretical description of metal pad roll instability. We adapt the stability model that H19 designed for two-layer systems to the three-layer, battery case. This theory roughly follows the same steps as in H19 and is explained in §2. In §3, we apply the theory to different LMBs set-ups. We study the Mg||Sb cells of Weber *et al.* (2017*b*,*a*), the cells of Horstmann *et al.* (2018) and in both sections, we compare our theory to some new direct numerical simulations, done with two different multiphase MHD solvers, OpenFOAM and SFEMaNS (see Guermond *et al.* (2007, 2009); Nore *et al.* (2016); Cappanera *et al.* (2018) for detailed information on the numerical methods). Tucs *et al.* (2018*a*) have studied metal pad roll in a square Na||Bi cell and we have found it interesting to apply our theory to a cylindrical analogue of this cell. Finally, we show that our theory can be used to estimate the stability regions of different liquid metal batteries, with different geometry and materials. Inspired by Tucs *et al.* (2018*b*), we compute critical magnetic fields $B_{z,c}$ for the onset of instability in a hypothetical, large and shallow 10^5 A cell. We also map the domain of stability in a size of cell vs. current density chart. Such charts can serve as a first order estimate to know where future, large scale LMBs would be stable with respect to metal pad roll instability.

2. Metal pad roll stability theory

2.1. *Base state*

We model metal pad roll (MPR) instability in a three layer, cylindrical liquid metal battery (LMB) and use the notations of figure 1-(a) that shows the base state. The cylinder has radius R and the height of the three layers is H_i with $i = 1, 2, 3$. We use cylindrical coordinates (r, θ, z) and basis $(\boldsymbol{e_r}, \boldsymbol{e_\theta}, \boldsymbol{e_z})$. The electrical conductivity, the density and the kinematic viscosity are denoted σ_i, ρ_i, ν_i in layers $i = 1, 2, 3$. We will denote density differences

$$\Delta\rho_{12} = \rho_2 - \rho_1 \quad , \quad \Delta\rho_{23} = \rho_3 - \rho_2 \tag{2.1}$$

Standard gravity is g and we ignore surface tension in this study. We suppose a base state with all fluids at rest separated by planar interfaces at $z = 0$ (1|2 interface) and $z = -H_2$ (2|3) interface. The base state pressure P_i is hydrostatic, $\partial_z P_i = -\rho_i g$ and continuous at the interfaces, so $(P_1, P_2, P_3) = P_0 + (-\rho_1 g z, -\rho_2 g z, -\rho_3 g(z + H_2) + \rho_2 g H_2)$ with P_0 denoting an arbitrary ambient pressure. We imagine solid electrodes connecting to the liquids at $z = H_1$ and $z = -H_2 - H_3$ with an electrical conductivity that is supposed significantly smaller compared to that of the liquid metals in zones 1 and 3. A perfectly homogenous electrical current with density $\boldsymbol{J} = J\boldsymbol{e}_z$ runs vertically through the three layers. The base-state electrical potential Φ_i is defined by $J = -\sigma_i \partial_z \Phi_i$ and is continuous at the interfaces. This yields $(\Phi_1, \Phi_2, \Phi_3) = \Phi_0 + J(-\sigma_1^{-1} z, -\sigma_2^{-1} z, -\sigma_3^{-1}(z + H_2) + \sigma_2^{-1} H_2)$ inside the cell, with Φ_0 arbitrary. A uniform vertical magnetic field $\boldsymbol{B}^e = B_z \boldsymbol{e}_z$ is externally applied to the cell, the total magnetic field is $\boldsymbol{B} = (\mu_0 J r/2)\boldsymbol{e}_\theta + B_z \boldsymbol{e}_z$. In the following we refer to the unperturbed fluid volumes as $\mathcal{V}_1, \mathcal{V}_2, \mathcal{V}_3$. The boundaries of these fluid domains are $\delta\mathcal{V}_1, \delta\mathcal{V}_2, \delta\mathcal{V}_3$ and include the solid walls $\Sigma_1, \Sigma_2, \Sigma_3$ and the interfaces $z = 0$ and $z = -H_2$ are $\mathcal{S}_{12}$ and $\mathcal{S}_{23}$.

2.2. *Linear perturbation problem*

We are interested in the linear stability of the previously defined base state. We denote $(\boldsymbol{u_i}, p_i, \boldsymbol{b_i}, \boldsymbol{j_i}, \varphi_i)$, the linear perturbations of flow, pressure, magnetic field, current density and electrical potential. The linearised magnetohydrodynamical equations for the perturbations are

$$\rho_i \partial_t \boldsymbol{u_i} + \boldsymbol{\nabla} p_i = \boldsymbol{J} \times \boldsymbol{b_i} + \boldsymbol{j_i} \times \boldsymbol{B} + \rho_i \nu_i \boldsymbol{\Delta} \boldsymbol{u}_i \tag{2.2a}$$

$$\boldsymbol{\nabla} \cdot \boldsymbol{u}_i = 0 \tag{2.2b}$$

$$\boldsymbol{j}_i = \sigma_i(-\boldsymbol{\nabla}\varphi_i + \boldsymbol{u}_i \times \boldsymbol{B}) \tag{2.2c}$$

$$\boldsymbol{\nabla} \cdot \boldsymbol{j_i} = 0 \tag{2.2d}$$

The magnetic field perturbation $\boldsymbol{b}_i$ further satisfies $\boldsymbol{\nabla} \times \boldsymbol{b}_i = \mu_0 \boldsymbol{j}_i$ and $\boldsymbol{\nabla} \cdot \boldsymbol{b}_i = 0$. It is not of much interest to calculate this field, since the term $\boldsymbol{J} \times \boldsymbol{b_i}$ is not destabilising in the perturbative limit that we will consider here (see H19). The solid wall Σ of the cylinder is impermeable

$$\boldsymbol{u}_i \cdot \boldsymbol{n}_i = 0|_\Sigma. \tag{2.3}$$

We denote $\boldsymbol{n}_i$ the unit normal vector. In viscous fluids, tangential flow also vanishes at the boundary $\boldsymbol{n}_i \times \boldsymbol{u}_i|_\Sigma = 0$. We locate the deformed interfaces at $z = \eta_{12}(r, \theta, t)$ and $z = \eta_{23}(r, \theta, t)$. The linearised kinematic and dynamic boundary conditions are

$$\partial_t \eta_{12} = u_{1,z}|_{z=0} = u_{2,z}|_{z=0} \tag{2.4a}$$

$$\partial_t \eta_{23} = u_{2,z}|_{z=-H_2} = u_{3,z}|_{z=-H_2} \tag{2.4b}$$

$$\Delta\rho_{12} g \eta_{12} = p_2|_{z=0} - p_1|_{z=0} \tag{2.4c}$$

$$\Delta\rho_{23} g \eta_{23} = p_3|_{z=-H_2} - p_2|_{z=-H_2} \tag{2.4d}$$

In viscous fluids, tangential flow and tangential viscous constraint are continuous. Electrical boundary conditions on the solid walls are

$$\boldsymbol{j}_i.\boldsymbol{n}_i = 0|_{\Sigma}. \tag{2.5}$$

This relation is exact on the radial sidewall and a good approximation when the solid electrodes that we imagine above layer 1 and under layer 3, have an electrical conductivity that is significantly lower than σ_1 and σ_3. At the interfaces we express that the total normal electrical current $(\boldsymbol{J}+\boldsymbol{j})\cdot\boldsymbol{n}$ and total electrical potentiel $\Phi+\varphi$ are continuous. After linearisation, this yields :

$$j_{2,z}|_{z=0} - j_{1,z}|_{z=0} = j_{3,z}|_{z=-H_2} - j_{2,z}|_{z=-H_2} = 0 \tag{2.6a}$$

$$\varphi_2|_{z=0} - \varphi_1|_{z=0} = J(\sigma_2^{-1} - \sigma_1^{-1})\eta_{12} \tag{2.6b}$$

$$\varphi_3|_{z=-H_2} - \varphi_2|_{z=-H_2} = J(\sigma_3^{-1} - \sigma_2^{-1})\eta_{23} \tag{2.6c}$$

Surface elevations η_{12}, η_{23} cause jumps in the electrical potential perturbation φ if the conductivity of the layers is different. This physical ingredient really is essential for MPR instability to occur.

The linear stability problem is now entirely defined. We may search solutions in which arbitrary field components f grow as $f = \widehat{f}e^{st}$. In the following, hatted variables, $\widehat{f}$ always represent the spatial structure of a field, $s \in \mathbb{C}$ is a complex growth rate. Instability requires $\mathrm{Re}(s) > 0$.

2.3. *Instability mechanism in three-layer systems*

Before we zoom into the technical calculation of the growth rate of the waves, let us have a look at the physics of the instability mechanism. In figure 2 we illustrate three typical situations that can occur in three layer systems. Imagine to start with, a gravity wave that rotates as indicated by the black arrow and has instantaneous interface deformation of three typical types. Many liquid metal batteries have much larger density jumps on the bottom interface, $\Delta\rho_{12} \ll \Delta\rho_{23}$ and the result is that the waveform will practically leave the lower interface undeformed, as in case (a). This case is called the decoupled case by Horstmann *et al.* (2018). Some batteries have $\Delta\rho_{12} \approx \Delta\rho_{23}$ and then we can have either (b) anti-symmetrically deformed interfaces or (c) symmetrically deformed interfaces.

In the top row of figure 2, we suggest the instantaneous flow, $\boldsymbol{u}$ using green arrows, together with the spatial variation of total electrical current, $\boldsymbol{J}+\boldsymbol{j}$ using red arrows. To understand the direction of $\boldsymbol{u}$ just imagine how material needs to be displaced for the wave to rotate in the direction of the black arrow. To understand the structure of $\boldsymbol{J}+\boldsymbol{j}$, just take into account that the electrolyte is a bad conductor and that the current will be intensified (thicker arrows) near the narrower parts of the electrolyte.

In the bottom row of figure 2, we suggest the typical loops that are followed by current deviation $\boldsymbol{j}$. In cases (a) and (b), we expect a single $\boldsymbol{j}$-loop but in case (c), we will rather have a pair of $\boldsymbol{j}$-loops to be able to create a small horizontal current deviation defect within the inclined electrolyte layer. Having these loops in mind, we can now draw the instantaneous direction of Lorentz force, $\boldsymbol{j}\times\boldsymbol{B}^e$ (light green arrows). If the Lorentz force is to be destabilizing, it has to align more or less with the instantaneous flow as $\boldsymbol{u}\cdot(\boldsymbol{j}\times\boldsymbol{B}^e) > 0$ indeed indicates that power is being injected into the flow. This power injection apparently is very different in cases (a), (b) and (c).

Let us discuss case (a) first. The figure suggests that $\boldsymbol{u}$ indeed aligns with $\boldsymbol{j}\times\boldsymbol{B}^e$ in the top layer, so power is indeed injected into the wave in this layer. As the same figure can be drawn at any rotated position, we can expect a permanent injection of power and hence an amplification. In this battery type with $\Delta\rho_{12} \ll \Delta\rho_{23}$, the bottom layer is almost at rest and

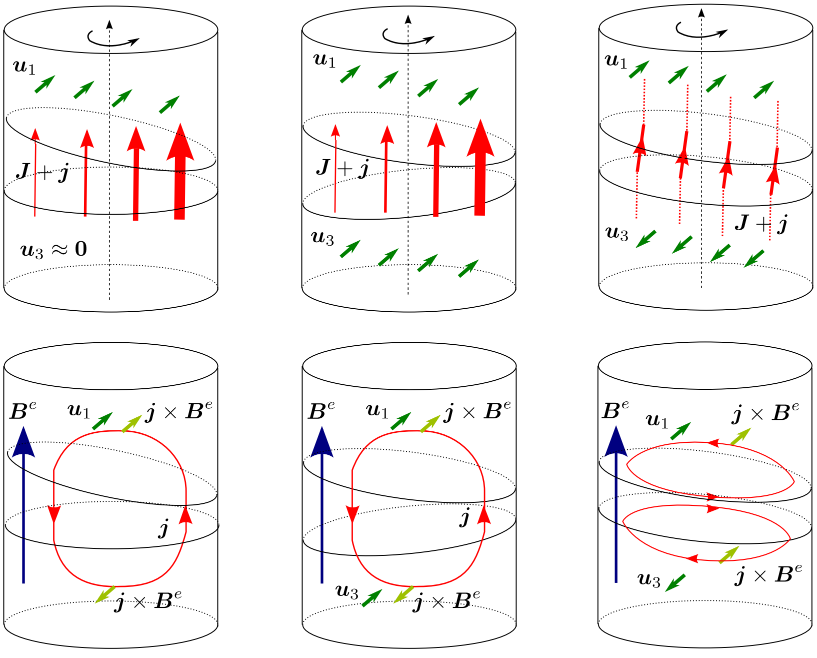

(a) (b) (c)

Figure 2: Metal pad roll instability mechanism in batteries, in three characteristic situations. Top row shows interface deformations, instantaneous flows for a rotating wave and current deflections. The bottom row shows perturbed current loops and compares the direction of Lorentz force $\boldsymbol{j} \times \boldsymbol{B}^e$ to that of $\boldsymbol{u}$. In many LMBs, $\Delta\rho_{12} \ll \Delta\rho_{23}$ and we expect a waveform as in (a) where the bottom interface remains almost flat. When $\Delta\rho_{23} \approx \Delta\rho_{12}$ other waveforms are possible, anti-symmetrical waveforms (b) or symmetrical waveforms (c).

hence, with $\boldsymbol{u}_3 \approx \boldsymbol{0}$, this layer will not be receiving much power from the Lorentz force. The result is that metal pad roll will be very much as in a two-layer system, a feature that is already known since the simulations of Weber *et al.* (2017*b*,*a*) for Mg||Sb batteries. Notice that the direction of rotation of the wave is crucial for amplification. If we invert the rotation direction, $\boldsymbol{u}$ changes sign and hence anti-aligns with $\boldsymbol{j} \times \boldsymbol{B}^e$ so this wave would be electromagnetically damped.

When $\Delta\rho_{12} \approx \Delta\rho_{23}$ other waveforms are possible as we know from Horstmann *et al.* (2018), but power injection may be rather different in this situation. On the typical $\boldsymbol{j}$-loops, it is easy to draw the instantaneous direction of the Lorentz force $\boldsymbol{j} \times \boldsymbol{B}^e$. Interestingly, it seems that $\boldsymbol{u} \cdot (\boldsymbol{j} \times \boldsymbol{B}^e) > 0$ in the top layer, but $\boldsymbol{u} \cdot (\boldsymbol{j} \times \boldsymbol{B}^e) < 0$ in the bottom layer. Energy is injected into this rotating wave in the top layer, but withdrawn from the wave in the bottom layer. This situation of opposing power transfers is a particularity of the metal pad roll instability with three layers and these symmetrical or anti-symmetrical waveforms. It seems to suggest that, with $\Delta\rho_{12} \approx \Delta\rho_{23}$, we can end up with a very weak metal pad roll instability. Below, we will show more formally that this is indeed the case.

2.4. *Perturbative solution*

2.4.1. *Main idea*

Let us now present our formal calculation of the growth rate of the instability. When both the Lorentz and viscous forces are small in comparison to inertia and pressure forces, we can model their effect perturbatively. At lowest order, we start by finding free-gravity waves and the accompanying electrical current and potential perturbations. Next we calculate the complex growth rate as :

$$s = \mathrm{i}\omega + \underbrace{\lambda + \mathrm{i}\delta}_{\text{small shift}} \tag{2.7}$$

The leading order value of the complex growth rate s is set by $i\omega$ where $\omega \in \mathbb{R}$ is the frequency of free inviscid gravity waves. Small viscosity and small Lorentz forces cause a complex shift in s, that we may further split in real and imaginary parts as $\lambda + i\delta$. The term $\mathrm{i}\delta$ is not very interesting as it corresponds to a small, real frequency shift. As in H19, it is partly caused by viscosity and partly by the Lorentz-force due to the azimuthal or horizontal magnetic field $B_\theta = \mu_0 Jr/2$. In this article, we will not calculate this frequency shift δ. Our focus will entirely be on the real growth rate λ as this is the term that characterises the growth or decay of a wave. We evaluate λ as the sum of three independent terms:

$$\lambda = \lambda_v + \lambda_{visc} + \lambda_{vv} \tag{2.8}$$

The term $\lambda_v \sim JB_z$ is the only one that can be positive and it is the one that relates to the Sele-instability mechanism, discussed in the previous section. The term $\lambda_{visc} < 0$ is the viscous damping of the wave. This damping is due to dissipation in the thin Stokes layers that exist at the solid boundaries *and* near the interfaces. The term $\lambda_{vv} < 0$ is the magnetic damping due to induction in the top and bottom metals. Proportional to $\sim B_z^2$ it is very small for low imposed magnetic fields. In the following sections we calculate all three terms λ_v, λ_{visc} and λ_{vv} separately.

2.4.2. *Hydrodynamic problem at leading order: gravity waves*

The perturbative approach starts with a characterisation of the leading order hydrodynamical wave problem. Without Lorentz and viscous forces, we need to solve :

$$\rho_i \partial_t \boldsymbol{u_i} + \boldsymbol{\nabla} p_i = 0, \quad , \quad \boldsymbol{\nabla} \cdot \boldsymbol{u}_i = 0 \tag{2.9}$$

with the boundary conditions (2.4). This three-layer wave problem was already studied in detail by Horstmann *et al.* (2018). Here we use slightly different notations to remain as close as possible to the presentation of H19 that we wish to extend. Our solution is

$$[\boldsymbol{u}_i, p_i, \eta_{12}, \eta_{23}] = [\widehat{\boldsymbol{u}}_i, \widehat{p}_i, \widehat{\eta}_{12}, \widehat{\eta}_{23}] e^{\mathrm{i}\omega t} \tag{2.10}$$

with a flow that is potential: $\widehat{\boldsymbol{u}}_i = \boldsymbol{\nabla}\widehat{\phi}_i$ and $\nabla^2 \widehat{\phi}_i = 0$. The hydrodynamic potentials and interface shapes of the waves are defined by

$$\widehat{\phi}_1 = \frac{\omega R}{k} a \frac{\cosh(k(z - H_1))}{\sinh(kH_1)} J_m(kr) e^{\mathrm{i}m\theta} \tag{2.11a}$$

$$\widehat{\phi}_2 = \frac{\omega R}{k} \left(b \frac{\cosh(kz)}{\sinh(kH_2)} - a \frac{\cosh(k(z + H_2))}{\sinh(kH_2)} \right) J_m(kr) e^{\mathrm{i}m\theta} \tag{2.11b}$$

$$\widehat{\phi}_3 = -\frac{\omega R}{k} b \frac{\cosh(k(z + H_2 + H_3))}{\sinh(kH_3)} J_m(kr) e^{\mathrm{i}m\theta} \tag{2.11c}$$

and

$$\widehat{\eta}_{12} = R\,\mathrm{i}aJ_m(kr)e^{\mathrm{i}m\theta} \tag{2.11d}$$
$$\widehat{\eta}_{23} = R\,\mathrm{i}bJ_m(kr)e^{\mathrm{i}m\theta}. \tag{2.11e}$$

Pressure relates to hydrodynamic potential by $\widehat{p_i} = -\mathrm{i}\omega\rho_i\widehat{\phi_i}$. In these formulas J_m represents a Bessel function of the first kind, $m \in \mathbb{N}$ the azimuthal wavenumber that can be considered positive. k is the radial wavenumber that takes the discrete values $k = \kappa_{mn}/R$ with κ_{mn} the n-th zero of $J'_m(\kappa_{mn}) = 0$. The solution (2.11) has impermeability on the solid walls built in and also the kinematic boundary conditions are already satisfied on the interfaces. The non-dimensional amplitudes a, b are still undetermined but they are non-trivially related by the algebraical system that is found by expressing the dynamic boundary conditions (2.4c) and (2.4d):

$$\begin{pmatrix} \dfrac{\omega_{12}^2}{\omega^2} - 1 & \dfrac{\rho_2}{\overline{\rho}_{12}\sinh(kH_2)} \\ \dfrac{\rho_2}{\overline{\rho}_{23}\sinh(kH_2)} & \dfrac{\omega_{23}^2}{\omega^2} - 1 \end{pmatrix} \begin{pmatrix} a \\ b \end{pmatrix} = \begin{pmatrix} 0 \\ 0 \end{pmatrix} \tag{2.12}$$

Here and further, we note

$$\overline{\rho}_{12} = \frac{\rho_1}{\tanh(kH_1)} + \frac{\rho_2}{\tanh(kH_2)} \quad , \quad \overline{\rho}_{23} = \frac{\rho_2}{\tanh(kH_2)} + \frac{\rho_3}{\tanh(kH_3)} \tag{2.13a}$$
$$\omega_{12}^2 = \frac{\Delta\rho_{12}gk}{\overline{\rho}_{12}} \quad , \quad \omega_{23}^2 = \frac{\Delta\rho_{23}gk}{\overline{\rho}_{23}} \tag{2.13b}$$

The frequencies ω_{12} and ω_{23} are the wave-frequencies of the respective 2-layer systems. Existence of non-trivial solutions of (2.12) requires that

$$\left[\frac{1}{\omega^2} - \frac{1}{\omega_{12}^2}\right]\left[\frac{1}{\omega^2} - \frac{1}{\omega_{23}^2}\right] = \frac{\rho_2^2}{\overline{\rho}_{12}\overline{\rho}_{23}\sinh^2(kH_2)\omega_{12}^2\omega_{23}^2} \tag{2.14}$$

from which we can find that there are 2 possible values of ω^2:

$$\omega_\pm^2 = \left(\frac{1}{2}\left(\frac{1}{\omega_{12}^2} + \frac{1}{\omega_{23}^2}\right) \mp \frac{1}{2}\sqrt{\left(\frac{1}{\omega_{12}^2} - \frac{1}{\omega_{23}^2}\right)^2 + \frac{4}{\omega_{12}^2\omega_{23}^2}\frac{\rho_2^2}{\overline{\rho}_{12}\overline{\rho}_{23}}\frac{1}{\sinh^2(kH_2)}}\right)^{-1} \tag{2.15}$$

The sign ± chooses between the rapid frequency (+)-branch and the slow frequency (-)-branch and here we use the same notation as in Horstmann *et al.* (2018). Returning these two possible values of ω^2 to the original system (2.12), we find unique amplitude ratios $\epsilon = b/a$ for both the slow and rapid branches:

$$\epsilon_\pm = C \pm \sqrt{C^2 + D} \tag{2.16a}$$

with

$$C = \frac{1}{2}\left(\frac{\overline{\rho}_{12}}{\rho_2} - \frac{\Delta\rho_{12}}{\Delta\rho_{23}}\frac{\overline{\rho}_{23}}{\rho_2}\right)\sinh(kH_2) \quad , \quad D = \frac{\Delta\rho_{12}}{\Delta\rho_{23}} \tag{2.16b}$$

Fast waves always have $\epsilon_+ > 0$: both interfaces deform in phase, have their maxima and minima at the same azimuthal angle θ. This wave-form is referred to as symmetrical in Horstmann *et al.* (2018). Slow waves always have $\epsilon_- < 0$: both interfaces deform in phase opposition. Throughs of the upper 1|2 interface will be right above crests of the lower 2|3 interface. This wave-form is referred to as antisymmetrical in Horstmann *et al.* (2018). The

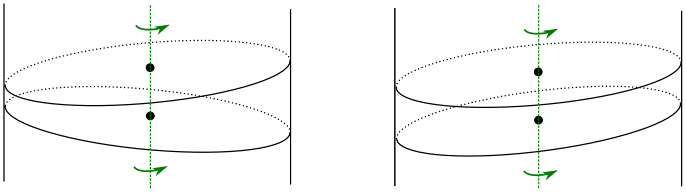

(a) slow $(1, 1, -)$ wave (b) rapid $(1, 1, +)$ wave

Figure 3: Illustration of the typical interface deformation for a rotating $(1, 1, \pm)$ wave. The green arrows suggest a positive rotation direction for a wave with $\omega < 0$. Top and bottom interface deformations are (a) in phase opposition for slow $-$ waves, the amplitude ratio $\epsilon_- < 0$. For rapid $+$ waves they are in phase (b), the amplitude ratio $\epsilon_+ > 0$.

difference is visually illustrated in figure 3 for the fundamental slow and fast waves that have $m = 1$ and $n = 1$.

In the following, we will refer to a particular type of wave by providing the triplet $(m, n, \pm)$. For each triplet $(m, n, \pm)$, we have unique values of $\omega_\pm$ and $\epsilon_\pm$. The frequency ω itself can take four values $+\omega_-, -\omega_-, +\omega_+, -\omega_+$. The sign of the frequency carries information on the direction of rotation of the wave. By convention we fix $m > 0$ and all field profiles are proportional to $\exp(i(m\theta + \omega t))$. Hence, with $\omega < 0$ we have a wave that rotates in the positive, $+\boldsymbol{e}_\theta$ direction. In figure 3, we illustrate how the typical interface deformations for the $(1, 1, -)$ and $(1, 1, +)$ waves move. For a wave with $\omega < 0$, this whole pattern rotates in the direction of $+\boldsymbol{e}_\theta$, suggested by the green arrow.

2.4.3. *Electrical problem at leading order, in the induction-less limit*

Waves on the interface cause a redistribution of electrical current. We calculate the leading order expression of $[\boldsymbol{j}_i, \varphi_i] = [\widehat{\boldsymbol{j}}_i, \widehat{\varphi}_i]e^{\mathrm{i}\omega t}$ in the induction-less, or static MHD limit. This means that we solve

$$\widehat{\boldsymbol{j}}_i = -\sigma_i \boldsymbol{\nabla} \widehat{\varphi}_i \qquad \boldsymbol{\nabla} \cdot \widehat{\boldsymbol{j}}_i = 0 \tag{2.17}$$

together with the boundary conditions (2.6). We find the solution:

$$\widehat{\varphi}_1 = \frac{JR}{\sigma_1} c \frac{\cosh(k(z - H_1))}{\sinh(kH_1)} J_m(kr) e^{im\theta} \tag{2.18a}$$

$$\widehat{\varphi}_2 = \frac{JR}{\sigma_2} \left(d \frac{\cosh(kz)}{\sinh(kH_2)} - c \frac{\cosh(k(z + H_2))}{\sinh(kH_2)} \right) J_m(kr) e^{im\theta} \tag{2.18b}$$

$$\widehat{\varphi}_3 = -\frac{JR}{\sigma_3} d \frac{\cosh(k(z + H_2 + H_3))}{\sinh(kH_3)} J_m(kr) e^{im\theta} \tag{2.18c}$$

All electrical boundary conditions on the solid walls are built-in and one can check that j_z is indeed continuous at $z = 0$ and $z = -H_2$. The coefficients c, d are still undetermined, but they are related to a, b by the algebraical equations that follow from the jump conditions on the electrical potential perturbations (2.6):

$$\begin{pmatrix} -A_{12} & (\sigma_2 \sinh(kH_2))^{-1} \\ (\sigma_2 \sinh(kH_2))^{-1} & -A_{23} \end{pmatrix} \begin{pmatrix} c \\ d \end{pmatrix} = \begin{pmatrix} \mathrm{i}(\sigma_2^{-1} - \sigma_1^{-1})a \\ \mathrm{i}(\sigma_3^{-1} - \sigma_2^{-1})b \end{pmatrix} \tag{2.19a}$$

Here we note

$$\begin{aligned} A_{12} &= \sigma_1^{-1} \tanh^{-1}(kH_1) + \sigma_2^{-1} \tanh^{-1}(kH_2), \\ A_{23} &= \sigma_2^{-1} \tanh^{-1}(kH_2) + \sigma_3^{-1} \tanh^{-1}(kH_3), \end{aligned} \tag{2.19b}$$

Explicit formulas of c and d as a function of a and b, can be calculated for arbitrary conductivities σ_i, but these formulas are not practical. To get deeper insights and much simpler expressions of c and d, we add a supplementary hypothesis: we will assume that layers 1 and 3 are much better conductors than layer 2, or more precisely that

$$\frac{\sigma_2}{\sigma_i} \ll \min\left(\left|\frac{\tanh(kH_i)}{\tanh(kH_2)}\right|, 1\right) \quad , \quad i = 1, 3 \tag{2.20}$$

In this limit, we can simplify the jump conditions (2.6b) and (2.6c) to :

$$\varphi_2|_{z=0} \approx J\sigma_2^{-1}\eta_{12} \quad , \quad \varphi_2|_{z=-H_2} \approx J\sigma_2^{-1}\eta_{23} \tag{2.21}$$

and find

$$c \approx \mathrm{i}\frac{b - a\cosh(kH_2)}{\sinh(kH_2)} \quad , \quad d \approx \mathrm{i}\frac{b\cosh(kH_2) - a}{\sinh(kH_2)} \tag{2.22}$$

One can immediately notice that these definitions of c, d are conductivity-independent. Just as in aluminium reduction cells, the perturbed current distribution is independent of σ_i if the difference in conductivity between the salt and the metal layers is big enough. This approximation is certainly justified in LMBs: the molten salt electrolyte has a conductivity σ_2 that is easily 10^4 lower than σ_1 and σ_3 in the electrodes. This approximation was also used in previous theoretical models for MPR instability in LMBs (Bojarevics & Tucs 2017; Zikanov 2018; Molokov 2018).

2.4.4. *Dissipationless growth rate, λ_v*

Having found the waves and the accompanying electrical current perturbations, we can calculate the inviscid, induction-less or more simply, the dissipation-less growth rate λ_v. This can be done by extending the perturbative approach of H19 (section 2.6.1) to three regions of fluid. It simply is enough to change all sums $\sum_{i=1,2}$ into sums that involve three layers, $\sum_{i=1,2,3}$. The formulas reduce in a similar way and so it makes little sense to repeat the lengthy asymptotic procedure here. We end up with a new three-layer formula for the growth rate λ_v that takes the following form:

$$\lambda_v = \frac{\mathcal{P}_v}{2\mathcal{K}} \quad \text{with} \quad \mathcal{P}_v = \sum_{i=1,2,3} \int_{\mathcal{V}_i} \widehat{\boldsymbol{u}}_i^* \cdot (\widehat{\boldsymbol{j}}_i \times B_z \boldsymbol{e}_z) dV \tag{2.23a}$$

and

$$\mathcal{K} = \sum_{i=1,2,3} \int_{\mathcal{V}_i} \rho_i ||\widehat{\boldsymbol{u}}_i||^2 dV = \left(\Delta\rho_{12} \int_{\mathcal{S}_{12}} |\widehat{\eta}_{12}|^2 \, dS + \Delta\rho_{23} \int_{\mathcal{S}_{23}} |\widehat{\eta}_{23}|^2 \, dS\right) g \tag{2.23b}$$

Interesting here is that $\mathcal{P}_v$ is structurally similar to the electromagnetic power that was mentioned in the discussion of the instability mechanism. The quantity $\mathcal{K}$ relates to the kinetic (or potential) energy of the wave in the wave. In some sense, expressing the solvability condition is not very different from expressing the mechanical energy theorem. Analytical evaluation of these integrals yields the following explicit formula

$$\lambda_v = \frac{m\omega}{\kappa_{mn}^2 - m^2} \frac{JB_z}{(\Delta\rho_{12} + \epsilon^2 \Delta\rho_{23}) g} \Xi \tag{2.24a}$$

with

$$\Xi = \frac{1}{2}\left[(\epsilon^2 - 1) + \left(\frac{\epsilon}{\sinh(kH_2)} - \frac{1}{\tanh(kH_2)}\right)\left(\frac{kH_1}{\sinh^2(kH_1)} + \frac{1}{\tanh(kH_1)}\right) - \left(\frac{\epsilon}{\sinh(kH_2)} - \frac{\epsilon^2}{\tanh(kH_2)}\right)\left(\frac{kH_3}{\sinh^2(kH_3)} + \frac{1}{\tanh(kH_3)}\right)\right] \quad (2.24b)$$

We have tested the validity of this formula by comparing it to numerical evaluations of the integrals. As in H19, we find the growth rate λ_v proportional to the positive wave-dependent factor $m\omega/(\kappa_{mn}^2 - m^2)$, a factor that balances force density JB_z over a gravitational force density $(\Delta\rho_{12} + \epsilon^2\Delta\rho_{23})g$. The number Ξ depends on the wave and on the geometry of the cell and it is not sign-definite. We will show that $\Xi = 0$ and hence $\lambda_v = 0$ is possible and that this is the result of exactly opposing electromagnetic power transfers, as we have mentioned in the discussion of figure 2.

To apply the previous formula, we start by fixing the pair of numbers m, n and next we compute $\epsilon_\pm$ and $\omega_\pm$. Four waves can exist, with different frequencies $\omega = \omega_-, -\omega_-, \omega_+, -\omega_+$ and respective amplitude ratios $\epsilon = \epsilon_-, \epsilon_-, \epsilon_+, \epsilon_+$. Instability requires $\lambda_v > 0$, equivalent to $\mathrm{Sgn}(m\omega JB_z\Xi) > 0$ or alternatively $\mathrm{Sgn}(m\omega) = \mathrm{Sgn}(JB_z\Xi)$. This means that out of 4 waves, only 2 can be destabilised: those rotating in a specific direction, those with the right sign of ω. Considering that our waves are proportional to $\exp(i(m\theta + \omega t))$ and that $m > 0$ by convention, we can predict the direction of rotation of the unstable wave as follows:

$$\mathrm{Sgn}(JB_z\,\Xi) = \begin{cases} +1 & , \quad \text{unstable waves have } m\omega > 0, \text{ rotate along } -\boldsymbol{e}_\theta \\ -1 & , \quad \text{unstable waves have } m\omega < 0, \text{ rotate along } +\boldsymbol{e}_\theta \end{cases} \quad (2.25)$$

When $\Xi = 0$ no wave is being destabilized. In this particular case, $\mathcal{P}_v = 0$, which means that the Lorentz force injects as much power as it is withdrawing. This possibility was already mentioned above in the discussion of the instability mechanism.

2.4.5. *Viscous dissipation, λ_{visc}*

Due to viscosity the waves experience a weak damping. The viscous damping formula for waves on a single layer of fluid layer in contact with air does not immediately extend to the case of multiple layers, mainly because we also have interfacial boundary layers. Indeed, the tangential inviscid wave-flow is not continuous across the interface and a thin viscous boundary layer forms at the interface.

Case & Parkinson (1957) used an energy balance to calculate the approximative viscous damping rate for wave on a single fluid layer. In H19, we have generalized this method to find damping rates of waves in a two-layer system. Here, we use it to calculate the damping rate of waves in the three-layer system. In practice, we just need to evaluate the following formula

$$\lambda_{visc} = \frac{\mathcal{D}'}{4\mathcal{K}} \quad \text{with} \quad \mathcal{D}' = -\frac{2}{\sqrt{2}}\left(\sum_{i=1,2,3} \rho_i\sqrt{\nu_i|\omega|}\int_{\delta\mathcal{V}_i} ||\widehat{\overline{\boldsymbol{u}}}_{i,\perp}||^2 dS\right) \quad (2.26)$$

and $\mathcal{K}$ as in (2.23*b*). The term $\mathcal{D}'$ is a boundary layer dissipation integral and in practice, we can calculate it as the sum of three surface integrals that cover δV_i, the boundaries of the three liquid zones (solid boundaries and interface). In the integrand, we find $\widehat{\overline{\boldsymbol{u}}}_{i,\perp}$, the leading order Stokes layer correction of the flow that is tangential to the boundary. We need to calculate these boundary layer corrections $\widehat{\overline{\boldsymbol{u}}}_{i,\perp}$ and this is done exactly as in H19. Let us introduce ζ a general notation for the coordinate that is everywhere normal to the boundary or interface, 0 at the boundary and inwardly increasing in the fluid i, e.g. for layer 1:

$$\zeta = \left\{ \begin{array}{rcl} R - r & , & \text{near } r = R \\ H_1 - z & , & \text{near } z = H_1 \\ z & , & \text{near } z = 0 \end{array} \right. \tag{2.27}$$

and similarly for the other layers. As usual with this type of approach, we do not model the complex boundary layer structure in the corner regions or near the moving contact lines. At leading order, $\widehat{\overline{\boldsymbol{u}}}_{i,\perp}$ needs to satisfy

$$\mathrm{i}\omega \widehat{\overline{\boldsymbol{u}}}_{i,\perp} = \nu_i \partial^2_{\zeta\zeta} \widehat{\overline{\boldsymbol{u}}}_{i,\perp} \tag{2.28}$$

on any portion of the boundary δV_i. This problem has two exponential solutions, but we only keep the solution that is exponentially decaying away from the boundary. Near the solid walls Σ_i, we express the no-slip condition for the total flow: $\widehat{\boldsymbol{u}}_{i,\perp} + \widehat{\overline{\boldsymbol{u}}}_{i,\perp}|_{\Sigma_i} = \boldsymbol{0}$. This yields the boundary layer correction

$$\text{near } \Sigma_i \ : \quad \widehat{\overline{\boldsymbol{u}}}_{i,\perp} = -\widehat{\boldsymbol{u}}_{i,\perp}|_{\Sigma_i} e^{-\Gamma\sqrt{\frac{|\omega|}{\nu_i}}\zeta} \tag{2.29}$$

We note $\Gamma = (1 + \mathrm{i}\,\mathrm{Sgn}(\omega))/\sqrt{2}$. Around the interfaces we express continuity of tangential viscous stress and continuity of tangential total flow, e.g. for the 1|2 interface:

$$\eta_1 \partial_z \widehat{\overline{\boldsymbol{u}}}_{2,\perp}|_{z=0} = \eta_2 \partial_z \widehat{\overline{\boldsymbol{u}}}_{2,\perp}|_{z=0} \quad , \quad \widehat{\boldsymbol{u}}_{1,\perp} + \widehat{\overline{\boldsymbol{u}}}_{1,\perp}|_{z=0} = \widehat{\boldsymbol{u}}_{2,\perp} + \widehat{\overline{\boldsymbol{u}}}_{2,\perp}|_{z=0} \tag{2.30}$$

This yields

$$\text{near } \mathcal{S}_{12} \ : \quad \widehat{\overline{\boldsymbol{u}}}_{1,\perp} = -\left(1 + \frac{\rho_1\sqrt{\nu_1}}{\rho_2\sqrt{\nu_2}}\right)^{-1} \left(\widehat{\boldsymbol{u}}_{1,\perp} - \widehat{\boldsymbol{u}}_{2,\perp}\right) e^{-\Gamma\sqrt{\frac{|\omega|}{\nu_1}}z} \tag{2.31a}$$

$$\widehat{\overline{\boldsymbol{u}}}_{2,\perp} = \left(1 + \frac{\rho_2\sqrt{\nu_2}}{\rho_1\sqrt{\nu_1}}\right)^{-1} \left(\widehat{\boldsymbol{u}}_{1,\perp} - \widehat{\boldsymbol{u}}_{2,\perp}\right) e^{\Gamma\sqrt{\frac{|\omega|}{\nu_2}}z} \tag{2.31b}$$

For the 2|3 interface at $z = -H_2$, calculations are similar and we find

$$\text{near } \mathcal{S}_{23} \ : \quad \widehat{\overline{\boldsymbol{u}}}_{2,\perp} = -\left(1 + \frac{\rho_2\sqrt{\nu_2}}{\rho_3\sqrt{\nu_3}}\right)^{-1} \left(\widehat{\boldsymbol{u}}_{2,\perp} - \widehat{\boldsymbol{u}}_{3,\perp}\right) e^{-\Gamma\sqrt{\frac{|\omega|}{\nu_2}}(z+H_2)} \tag{2.32a}$$

$$\widehat{\overline{\boldsymbol{u}}}_{3,\perp} = \left(1 + \frac{\rho_3\sqrt{\nu_3}}{\rho_2\sqrt{\nu_2}}\right)^{-1} \left(\widehat{\boldsymbol{u}}_{2,\perp} - \widehat{\boldsymbol{u}}_{3,\perp}\right) e^{\Gamma\sqrt{\frac{|\omega|}{\nu_3}}(z+H_2)} \tag{2.32b}$$

as boundary layer corrections. It is easy to see here that all the boundary layer corrections $\widehat{\overline{\boldsymbol{u}}}_{i,\perp}$ decrease over a typical distance $\sqrt{\nu_i/|\omega|}$ inward the fluid. This scale needs to be smaller than R or H_i if we want the boundary layer approach to make sense. The electrolyte layer is likely going to be the thinnest one, so one must verify that $\sqrt{\nu_2/|\omega|} \ll H_2$ prior to applying the damping formula. In all the results of the following sections, we verify this inequality.

With the boundary layer corrections calculated everywhere, we can evaluate the surface integrals that appear in the formula (2.26). We have found it useful to separate in λ_{visc} the interfacial contributions to the damping (suffix (i)) from solid wall contributions (suffix (s)) from the three distinct layers:

$$\lambda_{visc} = \lambda^{(i)}_{visc} + \lambda^{(s)}_{visc,1} + \lambda^{(s)}_{visc,2} + \lambda^{(s)}_{visc,3} \tag{2.33}$$

The contributions from the interfacial boundary layers are :

$$\lambda^{(i)}_{visc} = -\frac{1}{2\sqrt{2}}\frac{\omega^2\sqrt{|\omega|}}{(\Delta\rho_{12}+\epsilon^2\Delta\rho_{23})g}\sum_{j=1,2}\Lambda^2_{j\,j+1}\left(\frac{1}{\rho_j\sqrt{\nu_j}}+\frac{1}{\rho_{j+1}\sqrt{\nu_{j+1}}}\right)^{-1} \qquad (2.34a)$$

with

$$\Lambda_{12} = (\tanh^{-1}(kH_1)+\tanh^{-1}(kH_2)) - \epsilon/\sinh(kH_2) \qquad (2.34b)$$

$$\Lambda_{23} = \epsilon(\tanh^{-1}(kH_3)+\tanh^{-1}(kH_2)) - 1/\sinh(kH_2) \qquad (2.34c)$$

The solid wall contributions are :

$$\lambda^{(s)}_{visc,1} = -\frac{1}{2\sqrt{2}}\frac{1}{kR}\frac{\rho_1\omega^2\sqrt{\nu_1|\omega|}}{(\Delta\rho_{12}+\epsilon^2\Delta\rho_{23})g}\left[\frac{k(R-H_1)}{\sinh^2(kH_1)}+\frac{k^2R^2+m^2}{k^2R^2-m^2}\frac{1}{\tanh(kH_1)}\right] \qquad (2.35a)$$

$$\begin{aligned}\lambda^{(s)}_{visc,2} = {} & \frac{1}{2\sqrt{2}}\frac{1}{kR}\frac{\rho_2\omega^2\sqrt{\nu_2|\omega|}}{(\Delta\rho_{12}+\epsilon^2\Delta\rho_{23})g}\left[(\epsilon^2+1)\left(\frac{kH_2}{\sinh^2(kH_2)}-\frac{k^2R^2+m^2}{k^2R^2-m^2}\frac{1}{\tanh(kH_2)}\right)\right.\\ & \left.-2\epsilon\left(\frac{kH_2\cosh(kH_2)}{\sinh^2(kH_2)}-\frac{k^2R^2+m^2}{k^2R^2-m^2}\frac{1}{\sinh(kH_2)}\right)\right] \qquad (2.35b)\end{aligned}$$

$$\lambda^{(s)}_{visc,3} = -\frac{1}{2\sqrt{2}}\frac{1}{kR}\frac{\rho_3\omega^2\sqrt{\nu_3|\omega|}}{(\Delta\rho_{12}+\epsilon^2\Delta\rho_{23})g}\epsilon^2\left[\frac{k(R-H_3)}{\sinh^2(kH_3)}+\frac{k^2R^2+m^2}{k^2R^2-m^2}\frac{1}{\tanh(kH_3)}\right] \qquad (2.35c)$$

We have checked that these damping formulas yield the correct two layer limits of H19. As in H19, there always remains a degree of uncertainty in these formulas because the boundary layer regions near the moving menisci are not properly modeled. In reality they depend on wetting properties and although theoretical modeling is possible, see Viola & Gallaire (2018), this type of model is much more complex and not yet existing for two or three-layer systems.

2.4.6. *Magnetic dissipation, λ_{vv}*

In the calculation of λ_v, we have used an induction-less version of Ohm's law. This static approximation ignores that induced currents will arise due to the term $\sigma_i\boldsymbol{u}_i\times B_z\boldsymbol{e}_z$. This induction only occurs in the well-conducting metal layers and results in a weak magnetic damping λ_{vv} that we can calculate. In H19, it is explained how a correction to the electrical potential Ψ_i and current density $\mathcal{J}_i = \sigma_i(-\boldsymbol{\nabla}\Psi_i+\boldsymbol{u}_i\times B_z\boldsymbol{e}_z)$ needs to be added to have a total perturbed current $\boldsymbol{j}_i+\mathcal{J}_i$ that takes into account induction. Once this extra current perturbation $\mathcal{J}_i$ is known, we can found a quasi-static correction to the growth rate in the term

$$\lambda_{vv} = \frac{Q_{vv}}{2\mathcal{K}} \quad \text{with} \quad Q_{vv} = \sum_{i=1,2,3}\int_{\mathcal{V}_i}\widehat{\boldsymbol{u}}_i^*\cdot\left(\widehat{\mathcal{J}}_i\times B_z\boldsymbol{e}_z\right)\,dV, \qquad (2.36)$$

For arbitrary fluid combinations, there is no simple way to calculate the current correction $\widehat{\mathcal{J}}_i$. However, since we have assumed that only fluids 1 and 3 are good conductors, we can be sure that induction will only occur inside zones 1 and 3, such that $\widehat{\mathcal{J}}_2 = \boldsymbol{0}$ is a good approximation. This means that the quasi-static potential corrections are the solutions of

$$\begin{aligned}&\nabla^2\widehat{\Psi}_1 = 0 \quad , \quad \partial_z\widehat{\Psi}_1|_{z=0} = \partial_z\widehat{\Psi}_1|_{z=H_1} = 0 \quad , \quad \partial_r\widehat{\Psi}_1|_{r=R} = \widehat{u}_{\theta,1}|_{r=R}B_z \qquad (2.37)\\ &\nabla^2\widehat{\Psi}_3 = 0 \quad , \quad \partial_z\widehat{\Psi}_3|_{z=-H_2} = \partial_z\widehat{\Psi}_3|_{z=-H_2-H_3} = 0 \quad , \quad \partial_r\widehat{\Psi}_3|_{r=R} = \widehat{u}_{\theta,3}|_{r=R}B_z\end{aligned}$$

This problem was solved in one layer in H19. Here we can simply adapt the solution that was found there, to cover the case with 2 well conducting layers. We can then evaluate the integral Q_{vv} that provides access to the magnetic damping term. We find

$$\lambda_{vv} = \lambda_{vv,1} + \lambda_{vv,3} \tag{2.38}$$

with

$$\begin{aligned}
\lambda_{vv,1} = {} & \frac{\sigma_1 B^2}{\Delta\rho_{12} + \epsilon^2 \Delta\rho_{23}} \frac{\omega^2}{gk} \left[-\frac{1}{4} \left(\frac{1}{\tanh(kH_1)} + \frac{kH_1}{\sinh^2(kH_1)} \right) + \frac{1}{k^2R^2 - m^2} \right. \\
& \left. \times \left(\frac{m}{kH_1} + 4m^2 \sum_{j=1}^{\infty} \left(\frac{1}{j\pi} \right) \frac{k^3}{R(k^2 + (\frac{j\pi}{H_1})^2)^2} \frac{I_m(\frac{j\pi R}{H_1})}{I_{m-1}(\frac{j\pi R}{H_1}) + I_{m+1}(\frac{j\pi R}{H_1})} \right) \right] \qquad (2.39a) \\
\lambda_{vv,3} = {} & \epsilon^2 \frac{\sigma_3 B^2}{\Delta\rho_{12} + \epsilon^2 \Delta\rho_{23}} \frac{\omega^2}{gk} \left[-\frac{1}{4} \left(\frac{1}{\tanh(kH_3)} + \frac{kH_3}{\sinh^2(kH_3)} \right) + \frac{1}{k^2R^2 - m^2} \right. \\
& \left. \times \left(\frac{m}{kH_3} + 4m^2 \sum_{j=1}^{\infty} \left(\frac{1}{j\pi} \right) \frac{k^3}{R(k^2 + (\frac{j\pi}{H_3})^2)^2} \frac{I_m(\frac{j\pi R}{H_3})}{I_{m-1}(\frac{j\pi R}{H_3}) + I_{m+1}(\frac{j\pi R}{H_3})} \right) \right] \qquad (2.39b)
\end{aligned}$$

Here I_m and $I_{m\pm1}$ are modified Bessel functions. The sum over j quickly decays with increasing j and needs to be truncated in practice, when a machine precision is attained.

2.5. *Supplementary material: Jupyter notebook*

Although all the formulas for $\omega_\pm, \epsilon_\pm, \lambda_v, \lambda_{vv}, \lambda_{visc}$ are explicit, they remain nevertheless quite cumbersome. For this reason, we provide in the supplementary material a Jupyter notebook that encodes all the previous formulas. One can easily change the material properties and the geometrical parameters defining the battery, in a single parameter variable. The notebook then allows to calculate the growth rates of all the possible waves $(m, n, \pm)$. It also includes all the procedures that were used to produce most of the figures that appear in this article.

3. Applications

3.1. *Mg||Sb simulations of Weber* et al. *(2017*a,b*)*

MPR instability in a Mg||Sb battery was studied numerically by Weber *et al.* (2017*a*,*b*) in a small, centimeter-scale cell with geometrical parameters

$$(R, H_1, H_2, H_3) = (0.05, 0.045, 0.01, 0.045)\ \mathrm{m} \tag{3.1}$$

Material parameters are

$$\begin{aligned}
(\rho_1, \rho_2, \rho_3) &= (1577, 1715, 6270)\ \mathrm{kg\ m^{-3}} \\
(\sigma_1, \sigma_2, \sigma_3) &= (3.6 \times 10^6, 80, 8.7 \times 10^5)\ \mathrm{S\ m^{-1}} \\
(\nu_1, \nu_2, \nu_3) &= (6.7, 6.8, 2) \times 10^{-7} \mathrm{m^2\ s^{-1}} \qquad (3.2)
\end{aligned}$$

The particularity of Mg||Sb LMBs is that the density jump $\Delta\rho_{12} \ll \Delta\rho_{23}$. As a result, interfaces are decoupled and MPR instability is nearly as in a two-layer system. This was already shown in Weber *et al.* (2017*a*,*b*) and H19 showed that the two-layer stability theory precisely captures MPR instability in this cell. Nevertheless, this Mg||Sb cell still remains a useful test-case to our three-layer model. For a large number of waves $(m, n, \pm)$, we start by computing the numbers

$$\overline{\lambda}_v = \frac{\lambda_v}{JB_z \mathrm{Sgn}(\omega)} \quad , \quad \lambda_{visc} \quad , \quad \overline{\lambda}_{vv} = \frac{\lambda_{vv}}{B_z^2} \tag{3.3}$$

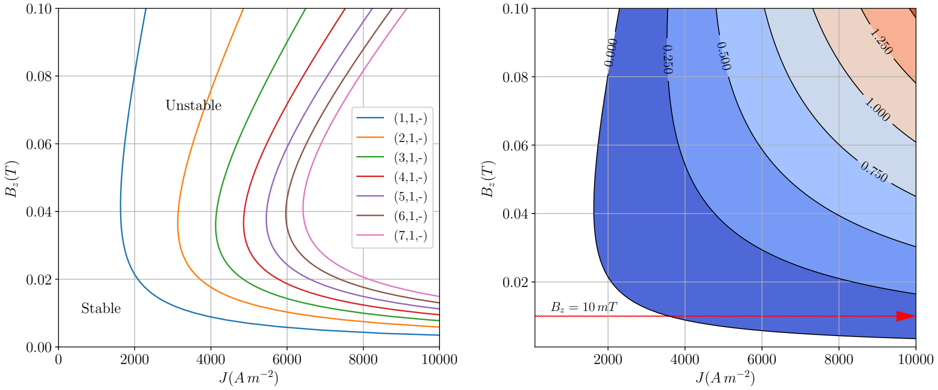

(a) (b)

Figure 4: Three-layer theory applied to the small Mg||Sb cell of Weber *et al.* (2017*a*,*b*). (a) Marginal stability curves for various waves in the $J - B_z$ plane. (b) Growth rate λ (s^{-1}) of the dominant, fundamental sloshing wave $(1, 1, -)$ in the JB_z-plane. Numerical growth rate measurements are available along the red line with $B_z = 10\,\mathrm{mT}$.

The growth rate is then calculated a posteriori for varying J and B_z using the formula $\lambda = |\overline{\lambda}_v|JB_z + \lambda_{visc} + \overline{\lambda}_{vv}B_z^2$. For given B_z, instability occurs when the current density exceeds a critical value $J > J_c$. According to our theory, this critical current density is

$$J_c = -\frac{\overline{\lambda}_{vv}B_z^2 + \lambda_{visc}}{|\overline{\lambda}_v|B_z} \tag{3.4}$$

In figure 4-(a), we show some theoretical marginal stability curves in the plane $J \in [0, 10000]\,\mathrm{Am}^{-2}$, $B_z \in [0, 0.1]\,\mathrm{T}$. In this part of the parameter space, we only find unstable $(m, 1, -)$ waves. Waves with higher radial label, $n > 1$ or $+$ waves from the fast branch are stable. The large-scale sloshing wave $(1, 1, -)$ is first destabilised and it is also the most unstable everywhere according to theory. This wave has frequency $\omega_- = 2.74\,\mathrm{s}^{-1}$ which corresponds to the value observed by Weber *et al.* (2017*a*,*b*). Its amplitude ratio is $\epsilon_- = -0.022$, which means that the lower 2|3 interface is practically undeformed, as expected. In figure 4-(b), we show the growth rate λ of this $(1, 1, -)$ wave in the $J - B_z$ plane. The shape of this growth rate diagram is similar to what we have seen in H19 and in Nore *et al.* (2021). Magnetic fields as high as $B_z = 0.1\,\mathrm{T}$ are very unlikely in reality, but allow us to see the possibly stabilizing effect of magnetic damping.

The simulations of Weber *et al.* (2017*a*,*b*) were done with OpenFOAM. We have done a small number of complementary simulations of the same set-up using SFEMaNS. These simulations confirm that the $(1, 1, -)$ wave is the most destabilised wave. A snapshot from a simulation with $J = 10000\,\mathrm{Am}^{-2}$ and $B_z = 10\,\mathrm{mT}$ is shown in 5-(a). We show the deformed interfaces, together with the flow intensity and some streamlines for the current perturbation $\boldsymbol{j}_{tot} - J\boldsymbol{e}_z$. The bottom 2|3 interface is indeed almost undeformed. Over time, this entire pattern rotates in the positive $+\boldsymbol{e}_\theta$ direction, in agreement with (2.25): $JB_z > 0$ and for this wave $\Xi = -2.39 < 0$. In figure 5-(b) we compare the theoretical growth rates to the numerical values measured in our simulations and to those reported by Weber *et al.* (2017*a*) for $B_z = 10\,\mathrm{mT}$ and variable J. For this low B_z, magnetic damping is negligible with respect to viscous damping ($\lambda_{vv} = -0.00389\,\mathrm{s}^{-1}$ compared to $\lambda_{visc} = -0.0674\,\mathrm{s}^{-1}$).

Overall the 3-layer theory agrees well with the numerical simulations for this Mg||Sb

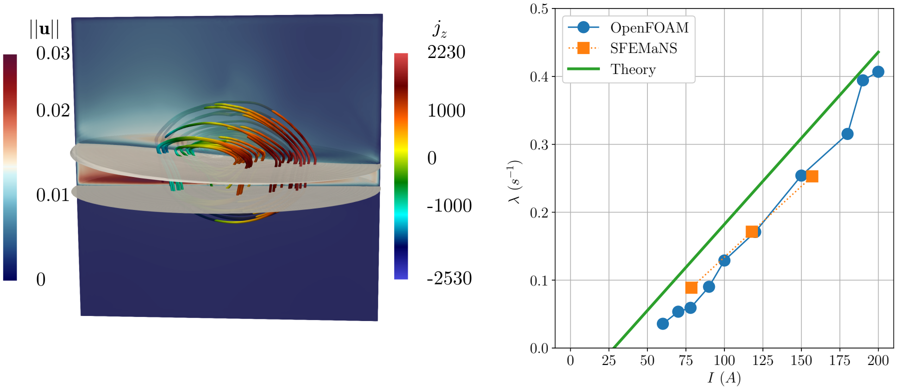

(a) (b)

Figure 5: (a) Snapshot of a $(1,1-)$ wave that grows in a small Mg||Sb battery simulated using SFEMaNS with $J = 10^4\,\mathrm{Am}^{-2}$ and $B_z = 10\,\mathrm{mT}$. We visualize the interfaces, the flow intensity and lines of the current density perturbation $\boldsymbol{j}_{tot} - J\boldsymbol{e}_z$ associated with the wave. (b) Growth rate of the instability as a function of current $I = J\pi R^2$ for fixed $B_z = 10\,\mathrm{mT}$. The theory compares well to growth rates measured in numerical simulations done with OpenFOAM and SFEMaNS.

battery, but not better than the 2-layer theory (see figure 14-b in H19). As in H19 and Nore *et al.* (2021), the theory suggests slightly larger growth rates and this indicates that viscous dissipation is a bit higher in the simulations. A weak amount of numerical dissipation is certainly present in all simulations, but also the theory for λ_{visc} remains perfectible.

3.2. *The three-layer simulations of Horstmann* et al. *(2018)*

As explained by Horstmann *et al.* (2018), not all LMBs behave as two-layer systems. When the density jump ratio $\Delta\rho_{12}/\Delta\rho_{23} \approx 1$, interfaces are coupled and all three layers can participate in the wave motion. We apply our theory to the three-layer set-ups studied numerically by Horstmann *et al.* (2018). The fluid layers have the same sizes as in the previous section:

$$(R, H_1, H_2, H_3) = (0.05, 0.045, 0.01, 0.045)\ \mathrm{m} \tag{3.5}$$

Material properties are allowed to vary more freely

$$\begin{aligned}(\rho_1, \rho_2, \rho_3) &= (\mathrm{variable}, 3000, 3500)\ \mathrm{kg\ m}^{-3}\\ (\sigma_1, \sigma_2, \sigma_3) &= (10^6, 500, 10^6)\ \mathrm{S\ m}^{-1}\\ (\nu_1, \nu_2, \nu_3) &= (6.7, 6.7, 6.7) \times 10^{-7}\ \mathrm{m}^2\ \mathrm{s}^{-1}\end{aligned} \tag{3.6}$$

and do not reflect a actual type of LMB. In their simulations, Horstmann *et al.* (2018) varied the top layer density $\rho_1 \in [500, 2950]\ \mathrm{kg\ m}^{-3}$. The external magnetic field was held fixed at $B_z = 10\,\mathrm{mT}$ and the total imposed current $I = J\pi R^2$ was varied in the interval $I \in [0, 500]\mathrm{A}$. All simulations were done with a small surface tension $\gamma_{1|2} = \gamma_{2|3} = 0.1\,\mathrm{N\,m}^{-1}$, that only weakly affects the waves and here is ignored in our theory.

As the density ρ_1 and applied total current I vary, different unstable waves can be observed in the simulations, see figure 6. In panel (a), we show the theoretical periods $T = 2\pi/\omega$ of the waves $(1, 1, +)$ and $(1, 1, -)$, as a function of $\Delta\rho_{12}/\Delta\rho_{23}$ along with the numerically measured periods in the late time state. For both low and high values of $\Delta\rho_{12}/\Delta\rho_{23}$, it is

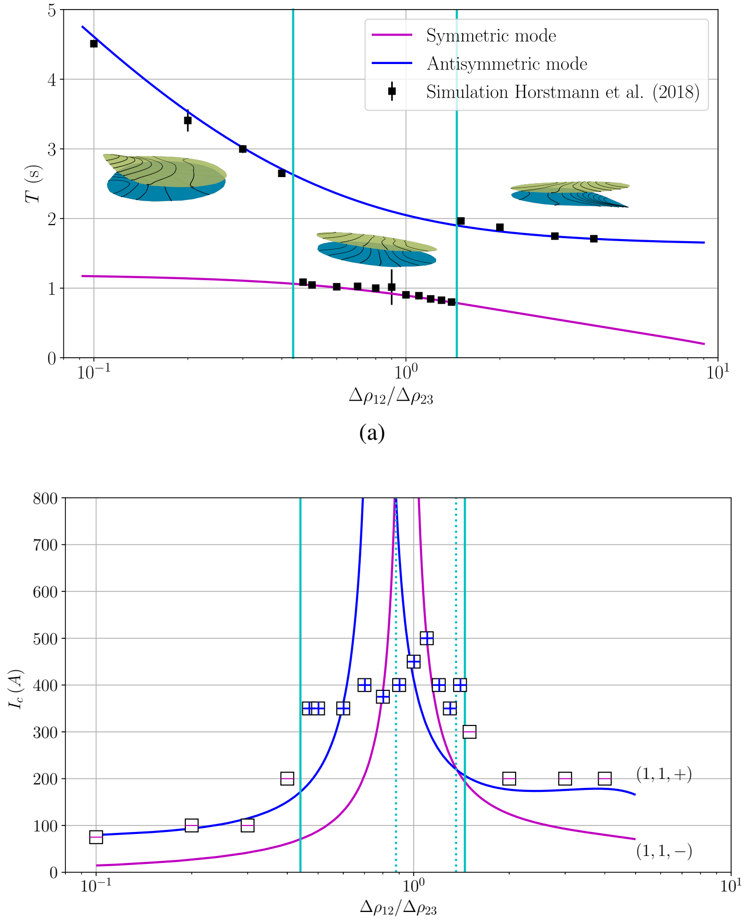

(a)

(b)

Figure 6: (a) The period $T = 2\pi/\omega$ of the unstable wave in the simulations of Horstmann *et al.* (2018) varies with $\Delta\rho_{12}/\Delta\rho_{23}$ and suggests that both $(1, 1, -)$ or $(1, 1, +)$ wave-modes can be selected. (b) Phase diagram in which we locate MPR-unstable simulations in the $\Delta\rho_{12}/\Delta\rho_{23}$ - I plane, + for the $(1, 1, +)$ wave and − for the $(1, 1, -)$ wave. The full lines correspond to the theoretical marginal instability curves of the $(1, 1, \pm)$- waves. Cyan vertical lines indicate frontiers between different selected wave-patterns according to the numerics (full lines) and our linear stability theory (dotted lines).

evident that the $(1, 1, -)$ wave is observed. For values of $\Delta\rho_{12}/\Delta\rho_{23}$ close to 1, the fast wave $(1, 1, +)$ is preferred. The inset figures show the typical interface deformations that are observed in the simulations. In this diagram, information on the value of the current I is lacking. In figure 6-(b), we locate the simulations that found unstable waves in the $\Delta\rho_{12}/\Delta\rho_{23}$ - I plane, using a + symbol when a $(1, 1, +)$ wave was observed and a − symbol when a $(1, 1, -)$ wave was observed. We clearly see the interval of dominance of each wave-mode and also that unstable $(1, 1, +)$ waves require significantly higher currents of order 400 A to become unstable in the simulations.

Let us now apply our theoretical model. We compute the numbers $\overline{\lambda}_v, \lambda_{visc}, \overline{\lambda}_{vv}$ for both waves $(1, 1, \pm)$ and for varying $\rho_1 \in [500, 2950]$ kg m^{-3}. We then use (3.4), to calculate the

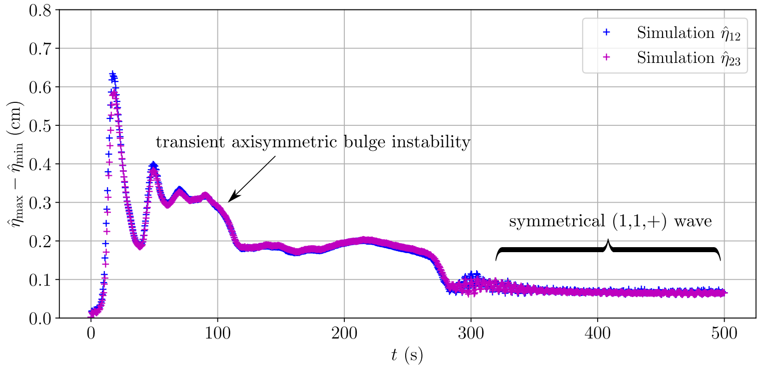

(a) Complex nonlinear transition, $\Delta\rho_{12}/\Delta\rho_{23} = 1$

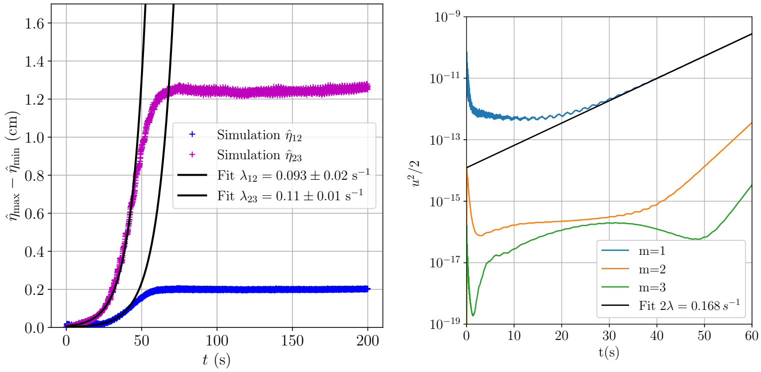

(b) OpenFOAM fit (c) SFEMaNS fit

Figure 7: Timeseries of interface deformation (OpenFOAM) and modal kinetic energy (SFEMaNS). (a) Example of nonlinear transition towards a state in which the $(1, 1, +)$ wave dominates ($I = 450$ A, $\rho_1 = 2500\,\mathrm{kg\ m^{-3}}$, $B_z = 10$mT . Growth rates cannot be measured here. (b-c) For lower currents we can measure growth rates using exponential fits on the maximal interface deformation in OpenFOAM or modal kinetic energy in SFEMaNS ($I = 200$ A, $\rho_1 = 1000\,\mathrm{kg\ m^{-3}}$, $B_z = 10$mT).

critical current $I_c = \pi R^2 J_c$, for both waves as a function of ρ_1. These critical currents define the marginal stability curves that are visible as full lines in figure 6-(b). One can immediately notice that the marginal instability curves move up to very high I when $\Delta\rho_{12}/\Delta\rho_{23} \approx 1$. All numerical simulations that yield $(1, 1, -)$ modes are above the theoretical marginal stability line. For $(1, 1, +)$ modes this is often the case but not always. The theoretical $\Delta\rho_{12}/\Delta\rho_{23}$ -interval where the $(1, 1, +)$ wave is dominant (distance between cyan dotted lines) is significantly narrower than what is observed in the simulations (distance between cyan full lines). The transition from $(1, 1-)$ to $(1, 1, +)$ modes near $\Delta\rho_{12}/\Delta\rho_{23} \approx 1.4$ is surprisingly well reproduced by the theory.

In figure 6-(b), we have compared late time nonlinear states with linear stability characteristics. This obviously is hazardous when the nonlinear evolution that leads to the late-time state is complex. Complex nonlinear transitions are observed in all the numerical simulations that result in $(1, 1, +)$ waves. In figure 7, one can see an example of such a transient in the simulation with $I = 450$ A, $\Delta\rho_{12}/\Delta\rho_{23} = 1$. We show the difference between the maximal and minimal interface deformation as a function of time, on both 1|2 and 2|3 interfaces. After an

ρ_1	$\Delta\rho_{12}/\Delta\rho_{23}$	λ (theory)	λ (OpenFOAM 1|2 fit)	λ (OpenFOAM 2|3 fit)	λ (SFEMaNS)
500	5	0.110	-	-	0.090
1000	4	0.098	0.093 ± 0.02	0.11 ± 0.01	0.084
2750	0.5	0.081	-	-	0.074
2800	0.4	0.139	0.168 ± 0.008	0.144 ± 0.02	0.131

Table 1: Comparison of the theoretical growth rate λ (s^{-1}) with numerically measured growth rates, for different values of ρ_1 (kg m^{-3}), $I = 200$ A, $B_z = 10$mT. Other geometrical and material parameters are specified in (3.11).

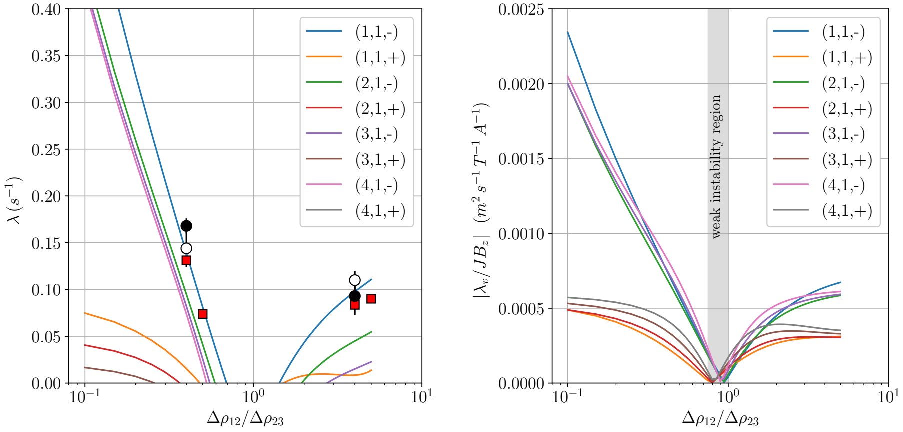

(a) (b)

Figure 8: (a) Growth rate of various waves $(m, 1, \pm)$ as a function of $\Delta\rho_{12}/\Delta\rho_{23}$ for $I = 200$A and several numerical measures. Near $\Delta\rho_{12}/\Delta\rho_{23} \approx 1$ there is a gap where all waves are stable. Datapoints from OpenFOAM simulations in white and black dots, data-points from SFEMaNS simulations in red squares (b) The relative dissipation-less growth rate $|\lambda_v|/JB_z$ as a function of $\Delta\rho_{12}/\Delta\rho_{23}$ vanishes sign near $\Delta\rho_{12}/\Delta\rho_{23} \approx 1$.

initial rapid growth of an axisymmetric bulge that was described in Horstmann *et al.* (2018), the signal gradually decays to settle into a low amplitude, symmetrical $(1, 1, +)$ wave at late time ($t > 300$s). This transition is clearly too nonlinear for linear stability theory to make much sense. For lower currents $I = 200$A, we have observed much simpler weakly nonlinear dynamics, in which a clear phase of exponential growth leads to a saturated $(1, 1, -)$ wave. For these simulations, we can obtain growth rate measurements. In OpenFOAM, we have done exponential fits on the maximal interface deformation data that is slightly noisy, see figure 7-(b) for an example. In SFEMaNS, we use a Fourier representation along the azimuth and this allows us to follow the growth of weak non-axisymmetric waves through modal kinetic energies, per azimuthal wavenumber m. Exponential fits on this data provide very precise measurements of the numerical growth rates, see figure 7-(c).

In Table 1 we gather the numerically measured growth rates and we compare them to the value estimated by our theory. As can be seen, the numerical growth rates match fairly well the theoretical growth rate values. As in H19, we see small differences between both solvers, OpenFOAM and SFEMaNS. In figure 8-(a), we add these numerically measured growth rates on a background of theoretical growth rate lines for various waves and as a function of $\Delta\rho_{12}/\Delta\rho_{23}$ (OpenFOAM fit in white and black dots, SFEMaNS fit in red squares). The quantitive agreement with theory can be visually appreciated. According to theory, the $(1,1,-)$ wave is the most unstable one over the entire $\Delta\rho_{12}/\Delta\rho_{23}$-interval. Interesting to notice here is that other waves $(m,1,-)$, with higher azimuthal wavenumber m are also destabilised at approximately similar rates when $\Delta\rho_{12}/\Delta\rho_{23} < 1$. Near $\Delta\rho_{12}/\Delta\rho_{23} \approx 1$ there are no unstable waves for this value of current, $I = 200$ A.

The existence of a "forbidden" region is certainly not due to an increased dissipation. It rather is the consequence of the fact that the dissipation-less growth rate λ_v vanishes at some point near $\Delta\rho_{12}/\Delta\rho_{23} \approx 1$. This can be seen better in figure 8-(b), that shows the relative dissipation-less growth rate $|\lambda_v|/JB_z$ for various waves as a function of $\Delta\rho_{12}/\Delta\rho_{23}$. Each wave has a unique value of $\Delta\rho_{12}/\Delta\rho_{23}$ for which $\lambda_v = 0$. Most slow branches $(-)$ reach 0 at $\Delta\rho_{12}/\Delta\rho_{23} \approx 1$. Most fast branches $(+)$ vanish near $\Delta\rho_{12}/\Delta\rho_{23} \approx 0.8$. Notice that the fact that λ_v can be zero also explains why the marginal stability curves in figure 6-(b) went up so high. Interestingly, we also understand better why the $(1,1,+)$ wave can be the most unstable one near $\Delta\rho_{12}/\Delta\rho_{23} \approx 1$: the $(1,1,-)$ wave has a nearly vanishing λ_v there.

We now show that the existence of weak instability regions in our theory relates to the opposing power transfers that were mentioned in the discussion of figure 2-(b) and (c). To show this more precisely, we start by looking back at the theoretical formula (2.24) for λ_v. In the present set-up, with $H_1 = H_3$, we can simplify the factor Ξ to

$$H_1 = H_3 \quad : \quad \Xi = \frac{1}{2}(\epsilon^2 - 1)\left[1 + \frac{1}{\tanh(kH_2)}\left(\frac{kH_1}{\sinh^2(kH_1)} + \frac{1}{\tanh(kH_1)}\right)\right] \tag{3.7}$$

This means that, in this cell with $H_1 = H_3$, we can have $\Xi = 0$ or $\lambda_v = 0$ when the interfaces are deformed in exactly symmetrical ($\epsilon = +1$) or anti-symmetrical ($\epsilon = -1$) ways. Using the theoretical expression (2.16) of the amplitude ratio ϵ, we can identify for which values of ρ_1 we have $\epsilon_\pm = \pm 1$:

$$\text{wave } (1,1,-) : \epsilon_- = -1 \text{ for } \rho_1 \approx 2523\,\text{kg m}^{-3},\ \Delta\rho_{12}/\Delta\rho_{23} = 0.954 \tag{3.8a}$$

$$\text{wave } (1,1,+) : \epsilon_+ = +1 \text{ for } \rho_1 \approx 2610\,\text{kg m}^{-3},\ \Delta\rho_{12}/\Delta\rho_{23} = 0.78 \tag{3.8b}$$

These values indeed coincide with the points where $\lambda_v = 0$ in figure 8-(b). Let us now rewrite the integral expression (2.23a) that defines λ_v in the following way

$$\lambda_v = \sum_{i=1,2,3} \int_{\mathcal{V}_i} \mathrm{p}_i \, dV \quad \text{with} \quad \mathrm{p}_i = \frac{\widehat{\boldsymbol{u}}_i^* \cdot (\widehat{\boldsymbol{j}}_i \times B_z)}{2\mathcal{K}} \tag{3.9}$$

In this formula, the field p_i indeed is a normalized power density. If $\mathrm{p}_i > 0$, the Lorentz force is locally pointing in the direction of the instantaneous flow and hence locally magnifying the wave. If $\mathrm{p}_i < 0$ the Lorentz force is on the contrary opposing to the instantaneous flow and hence it will locally damp the wave. In figure 9, we show the spatial distribution of p_i/JB_z in meridional planes for both types of waves $(1,1,-)$ in (a) and $(1,1,+)$ in (b), and for these very particular values of ρ_1 that yield $\lambda_v = 0$. We clearly observe perfectly antisymmetric distributions of power density that will cause $\sum_{i=1,2,3}\int_{\mathcal{V}_i} \mathrm{p}_i \, dV = 0$. Having $\lambda_v = 0$ indeed means that Lorentz force is destabilising in one half of the cell but stabilising in the other half. In other cells with $H_1 \neq H_3$, a similar balance of power can yield $\lambda_v = 0$, but not with $\epsilon_\pm = \pm 1$ exactly and for values of $\Delta\rho_{12}/\Delta\rho_{23}$ that can be different for each wave.

We conclude that our three-layer stability theory describes well the simulations of Horstmann *et al.* (2018). We cannot always explain why the $(1,1,+)$ wave appears in the late time state of the simulations since this is also the result of more complex nonlinear dynamics. On the growth rates that we were able to measure, we have reached quantitive agreement. Weak instability regions are present and influence mode selection.

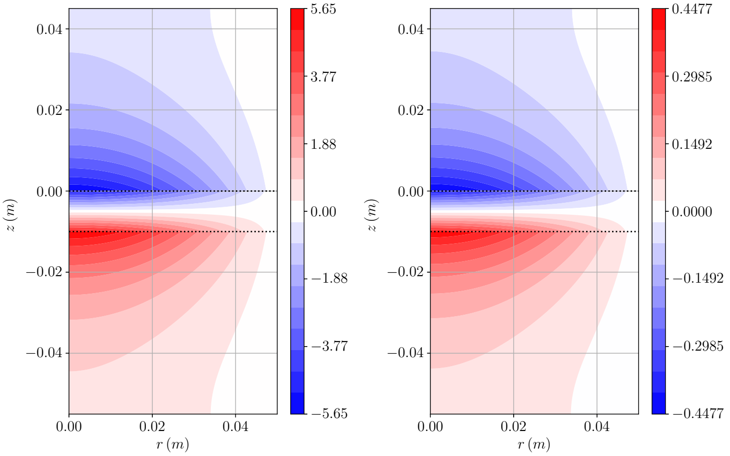

(a) (b)

Figure 9: The normalized power density p_i is perfectly anti-symmetrical in the special case of a vanishing dissipation-less growth rate. We show p_i/JB_z in the meridional plane of the cell of Horstmann *et al.* (2018) when $\lambda_\nu = 0$ exactly. (a) for the slow $(1,1,-)$ wave with $\epsilon_- = -1$ at $\rho_1 = 2523\,\mathrm{kg\ m^{-3}}$. (b) for the fast $(1,1,+)$ wave with $\epsilon_+ = 1$ at $\rho_1 = 2610\,\mathrm{kg\ m^{-3}}$.

3.3. *A cylindrical version of the Na||Bi cell of Tucs* et al. *(2018*a*)*

Tucs *et al.* (2018*a*) study metal pad roll instability inside discharging Na||Bi cells with square cross section and lateral sizes of $L_x = L_y = 0.2\,\mathrm{m}$. Square and cylindrical cells are very comparable for what concerns the MPR instability, because the rotating waves $(1,1,\pm)$ of the cylindrical cell are near to the most unstable superposition of standing waves, often labeled $(1,0)+(0,1)$. Therefore, we have found it interesting to apply our stability model to a cylindrical version of the cells studied by Tucs *et al.* (2018*a*). The geometry of our cylindrical equivalent is

$$(R, H_1, H_2, H_3) = (0.2/\sqrt{\pi}, \text{variable}, 0.01, , \text{variable})\ \mathrm{m} \tag{3.10}$$

Our cell has the same cross-section as that of Tucs *et al.* (2018*a*). We consider MPR instability in the interval $H_1 \in [0.02, 0.05]$ m, with $H_3 = 0.07\mathrm{m} - H_1$. Material properties are

$$\begin{aligned}(\rho_1,\rho_2,\rho_3) &= (831, 2540, 9720)\ \mathrm{kg\ m^{-3}}\\ (\sigma_1,\sigma_2,\sigma_3) &= (3.5\times10^6, 200, 0.69\times10^6)\ \mathrm{S\ m^{-1}}\\ (\nu_1,\nu_2,\nu_3) &= (0.26, 0.67, 1.1)\times10^{-6}\,\mathrm{m^2\ s^{-1}}\end{aligned} \tag{3.11}$$

As in Tucs *et al.* (2018*a*), we send a total current of $I = -130\,\mathrm{A}$ through the cell, equivalent to a current density $J = -3250\,\mathrm{Am^{-2}}$. We vary the magnetic field B_z. Our electrical boundary conditions on the side and the top and bottom plates are also identical to those of Tucs *et al.* (2018*a*). Our modeling of the viscous damping is however very different from that of Tucs *et al.* (2018*a*): they use the classical shallow fluid layer friction formula of Landau & Lifshitz (1987) that excludes damping in interfacial boundary layers.

In figure 10-(a), we show the theoretical growth rate λ of a function of H_3 for two different values of $B_z = 1\,mT$ and $B_z = 30\,mT$. Full lines show the general non-shallow theory, the dashed lines correspond to the shallow limits derived in appendix A.1. A shallow description is clearly adapted to this cell. For the low value of $B_z = 1\,mT$ that was used by Tucs *et al.*

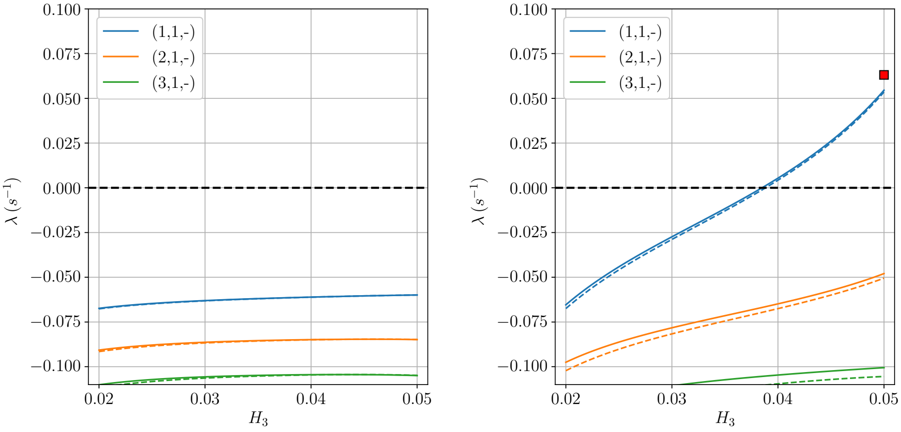

(a) $B_z = 1\,\mathrm{mT}$ (b) $B_z = 30\,\mathrm{mT}$

Figure 10: Theoretical growth rates λ as a function of H_3 for various waves in the cylindrical version of the Na||Bi cell of Tucs *et al.* (2018*a*). The general theory (full lines) is well approximated by the shallow limit formulas (dashed lines). (a) With low $B_z = 1$mT we do not find unstable waves. (b) A high magnetic field $B_z = 30$mT is necessary to destabilize a $(1, 1, -)$ mode and only in cells with large enough H_3. The red square is a data-point from a SFEMaNS simulation that is reasonably close to the theoretical curve.

(2018*a*), panel (a), our theory indicates a stable cell: all waves have $\lambda < 0$ for all values of H_3. According to our theory, MPR instability needs magnetic field intensities that are at least 13 times higher for the cell to become unstable in the studied H_3-interval. In figure 10-(b), we show the growth rate diagram with $B_z = 30\,mT$. For this significantly higher B_z, the magnetic damping term λ_{vv} is not negligible. Our theory suggests a stable cell for low H_3 and an unstable cell for large H_3. This wave has $\omega_- \approx 3.5\,\mathrm{s}^{-1}$ over the entire H_3 interval, which yields $f = \omega/2\pi \approx 0.56\,\mathrm{Hz}$ as frequency, a value that is remarkably close to the 0.55 Hz observed in the square cell by Tucs *et al.* (2018*a*).

According to our theory, the cylindrical version of the Na||Bi cell is much less unstable than the comparable square cell of Tucs *et al.* (2018*a*). This may be due to the fact that Tucs *et al.* (2018*a*) have used a viscous damping formula that is perhaps not really adapted. We have done a small number of direct numerical simulations using SFEMaNS to check our theoretical predictions. DNS of this set-up is incredibly difficult, because it needs to be very finely resolved. Boundary layers in which damping occurs have an estimated width of $\sqrt{\nu/\omega} \approx 0.5$mm. We use meridional grids that have minimal mesh-sizes that reach this fine scale which is more than 200 times smaller than the radius R of the cell. To handle this fine spatial resolution, we need time-steps that are smaller then 0.4 ms which means that we need no less than 5000 steps per wave-period ($\approx$ 2s). By initialising the calculation with the expected rotating wave, we are able to catch the exponential growth on a total integration time that covers only 10 rotation periods. For the set-up with $H_3 = 5$cm, this yields a growth rate measure of about $\lambda = 0.063\,\mathrm{s}^{-1}$. This data-point is added in figure 10-(b) and is reasonably close to the theoretical line. This is reassuring for our model.

3.4. *Critical magnetic field $B_{z,c}$ for* 10^5A *cells*

Tucs *et al.* (2018*b*) formulate a MPR stability theory for shallow large scale LMBs. In one of the numerical applications, the considered cell is supposed rectangular, with lateral sizes L_x =

# cell	Type	(ρ_1, ρ_2, ρ_3) in (kg m^{-3})	$\Delta\rho_{23}/\Delta\rho_{12}$
1	Li || Te	$(489, 2690, 5782)$	1.40
2	Na || Sn	$(801, 2420, 6740)$	2.67
3	Li || Bi	$(488, 2690, 9800)$	3.23
4	Li || Pb	$(488, 2690, 10463)$	3.53
5	Na|| Bi	$(831, 2549, 9720)$	4.17
6	Li || Zn	$(488, 1628, 6509])$	4.28
7	Li||Sn	$(495, 1644, 6877)$	4.55
8	Ca || Sb	$(1401, 1742, 6270)$	13.28
9	Ca || Bi	$(1434, 1803, 9720)$	21.46
10	Mg || Sb	$(1577, 1715, 6270)$	33.01

Table 2: Densities of the different layers and density jump ratio $\Delta\rho_{23}/\Delta\rho_{12}$, for the different LMBs studied by Tucs *et al.* (2018*b*).

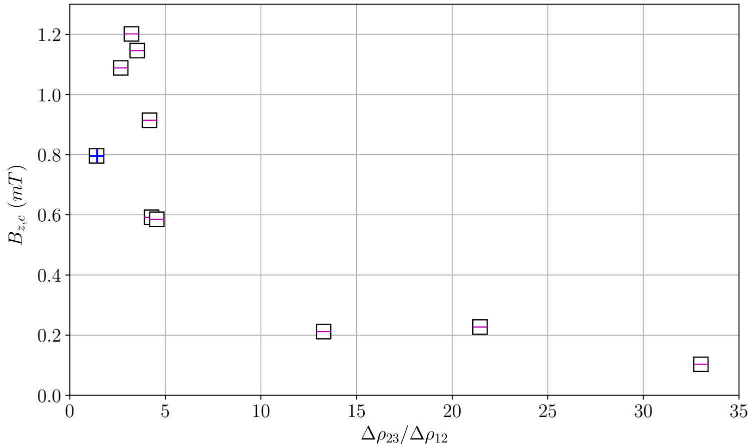

Figure 11: Critical magnetic field $B_{z,c}$ for the onset of MPR instability in large scale cylindrical LMBs of ten different types (see table 2) that alter the density jump ratio $\Delta\rho_{23}/\Delta\rho_{12}$. Symbols ± indicate that either $(1, 1, \pm)$ can be the first destabilised waves. $(R, H_1, H_2, H_3) = (3.03, 0.2, 0.04, 0.2)$ m, $I = 10^5$A.

8 m and $L_y = 3.6$ m and fluid layer heights are fixed at $(H_1, H_2, H_3) = (0.2, 0.04, 0.2)$ m. A total current of $I = 10^5$A passes through the cell, which is equivalent to a current density of $J = 3472$ Am^{-2}. Viscosity is held fixed at $\nu_i = 10^{-6}$ m^{2}s^{-1} everywhere. Ten different types of LMBs using metal-electrolyte-alloy combinations are compared and in table 2 we recall the densities of the three layers in these ten different LMB-types (data from Horstmann *et al.* (2018)). For each of these LMBs, (Tucs *et al.* 2018*b*, figure 7) calculate a critical vertical magnetic field $B_{z,c}$ for the onset of MPR instability.

We use our stability theory to calculate similar critical magnetic fields for the onset of MPR in cylindrical LMBs. We use the same heights of fluid layers (H_1, H_2, H_3) and the same total current I. Our cylindrical cell has $R = \sqrt{L_x L_y/\pi} = 3.03$ m to have an identical section, so we also have the same J. For a large variety of waves $(m, n, \pm)$ we calculate the relative dissipation-less growth rate $\overline{\lambda}_\nu = \lambda_\nu/JB_z$ and the viscous damping λ_{visc}. Magnetic damping $\lambda_{\nu\nu}$ can be ignored here because the fields B_z needed to destabilize such large cells are very

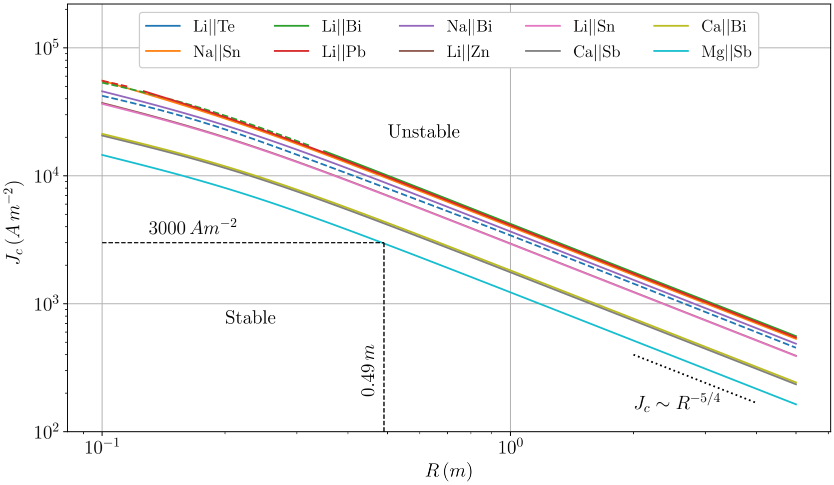

Figure 12: Critical current density J_c for the onset of MPR instability in different types of LMBs with varying radius R, fixed fluid layer heights $(H_1, H_2, H_3) = (0.2, 0.04, 0.2)$m. We use a worst case scenario estimate for the vertical magnetic field, $B_z \approx \mu_0 J\pi R/2$. Dashed lines when $(1, 1, +)$ waves are the first destabilized, full lines in the case of $(1, 1, -)$ waves.

low. Hence, we can estimate the critical magnetic field for the onset of MPR instability of a particular wave as

$$B_{z,c} = -\frac{\lambda_{visc}}{|J\overline{\lambda}_v|} \tag{3.12}$$

The lowest value $B_{z,c}$ defines the threshold magnetic field intensity. In cell 1, using the exotic combination of Li || Te, we find that the $(1, 1, +)$ wave is the first destabilised. Interestingly, this cell also has the ratio $\Delta\rho_{23}/\Delta\rho_{12}$ closest to unity. In all the other cells, 2 to 10, it is the $(1, 1, -)$ wave that has the lowest instability threshold. Typical values of $B_{z,c}$ are everywhere found within the $0.1 - 1.2$ mT range and just slightly above the dissipation-less values given by (Tucs *et al.* 2018*b*, figure 7). The critical magnetic field is lowest for the Mg||Sb cell, which is not really surprising. Of all LMBs, this one has the lowest density difference on one of its interfaces $\Delta\rho_{12} = 138$ kg m^{-3}. Deforming this interface simply requires less Lorentz force.

3.5. *Domains of stability in a radius - current density diagram*

Rather than using the magnetic field to express the instability threshold, we can also estimate the domain of stability of a cell with fixed layer heights in a $R - J$ plane. This allows to measure the critical size of a cell operating with a given current density. Let us give an example. We fix $(H_1, H_2, H_3) = (0.2, 0.04, 0.2)$ m as in the large scale study of Tucs *et al.* (2018*b*). We vary $R \in [0.1, 5]$m. Rather than taking some ad hoc, fixed value of B_z, we take into account that the magnetic field B_z is somehow being generated by the wires that bring the total current $I = J\pi R^2$ to the cell. In the worst case scenario, this suggests a magnetic field of order $B_z \approx \mu_0 I/2\pi R \approx \mu_0 JR/2$ (field at distance R from a wire carrying a current I). Alternatively speaking, in the worst case the vertical field is of the same order of magnitude as the azimuthal magnetic field B_θ created by the current density (this azimuthal field is not destabilizing, see H19). Using this estimate of B_z and the numbers λ_{visc} and $\overline{\lambda}_v = \lambda_v/JB_z$, we compute for each wave and for varying each cell radius the critical current density as

$$J_c \approx \sqrt{\frac{-2\lambda_{visc}}{|\bar{\lambda}_v|\mu_0 R}} \tag{3.13}$$

Magnetic damping is also ignored here. The wave with the lowest J_c defines the threshold. For the LMBs of table 2, this is most often the $(1,1,-)$ wave (full lines) but $(1,1,+)$ waves are also possible (dashed lines). In figure 12, we show this theoretical threshold current densities J_c for the different LMBs as a function of R. We observe a power-law $J_c \approx R^{-5/4}$ for large R. The Mg||Sb LMB clearly is the one that is most easily destabilised, closely followed by the Ca||Sb and Ca||Bi cells. For $J = 3000\,\mathrm{Am}^{-2}$, a typical value for the Mg||Sb battery, this formula locates the domain of stability at $R < 0.49\,\mathrm{m}$.

4. Conclusion

In this article we have presented a new linear stability theory for the metal pad roll instability in cylindrical LMBs, with three layers of stacked fluids. This theory extends the perturbative approach of H19 to the case of three layers and has all the same characteristics. It is obtained using perturbation methods, in non-shallow configurations and includes a precise model for viscous and magnetic dissipation.

The stability theory correctly captures the growth rates of the rolling wave observed by Weber *et al.* (2017*b*,*a*) in Mg||Sb cells. Our theory reproduces the fact that different wave modes, symmetrical and anti-symmetrical waves $(1,1,\pm)$ can be selected when $\Delta\rho_{12}/\Delta\rho_{23}$ is varied and shows that this is the consequence of a weak instability region that exists near $\Delta\rho_{12}/\Delta\rho_{23} \approx 1$. This weak instability region is the result of the fact that the Lorentz force can be destabilizing in top fluid layer but stabilizing in the bottom. This situation of opposing power injection and withdrawal is clearly only possible with three-layers of fluid and hence a particularity of the metal pad roll instability in batteries. According to our model, the cylindrical equivalent of the square Na||Bi cell of Tucs *et al.* (2018*a*) requires much higher imposed magnetic fields to become unstable, a difference that may be due to a different viscous damping model. Using our stability theory we can also estimate that the critical magnetic field needed to destabilize a hypothetically large shallow 10^5 A cell is of order of $B_z = 0.1 - 1\,\mathrm{mT}$ for several known LMB types. This critical magnetic field value is comparable to that given by Tucs *et al.* (2018*b*) for rectangular 10^5 A and is here uniquely due to viscous dissipation. Finally, we have shown how our theory can produce stability diagrams in a system size - current density plane. Such charts are useful to give a first order estimate of the regime of stability of an LMB with a given size.

One interesting perspective of this study is the possibility to study the effectiveness of passive control strategies. In industrial reduction cells, metal pad roll instability is avoided by taking thicker electrolyte layers. Using our theory, we can study whether this would be an effective control strategy in batteries too. From a numerical perspective, it would be interesting to study the interplay of metal pad roll instability and swirling electro-vortex flows (Bojarevics *et al.* 1989; Ashour *et al.* 2018; Herreman *et al.* 2021) that will also occur whenever current is injected by thinner solid electrodes.

The computational ressources used to realize the simulations using SFEMaNS were provided by GENCI-IDRIS (Grand Equipement National de Calcul Intensif), under the allocation 2021-0254. Declaration of interest: we declare no conflict of interest.

Appendix A. Special limits of the theory

It is easy to simplify the general theory in order to reach expressions valid in particular limits. The shallow limit, where all three layers are very thin with respect to the wavelength (or R), is particularly interesting for large scale shallow LMBs. The deep-shallow-deep limit is also interesting, because the theoretical formulas are significantly simpler.

A.1. *Shallow limit*

All our theoretical formulas for $\omega, \epsilon, \lambda_v, \lambda_{visc}, \lambda_{vv}$ can be written in a shallow limit for which $kH_i \ll 1$. For all but the magnetic damping term λ_{vv} it is sufficient to replace

$$\sinh(kH_i) \approx kH_i \quad , \quad \cos(kH_i) \approx 1 \quad , \quad \tanh(kH_i) \approx kH_i \tag{A 1}$$

in the general formulas. We have not found significant simplifications in the resulting formulas, so it makes no sense to rewrite explicit lengthy expressions for all quantities in this shallow limit. For the magnetic damping term, we can use

$$\lambda_{vv} = \frac{\omega^2}{gk}\left(\frac{\sigma_1 B^2}{\Delta\rho_{12} + \epsilon^2\Delta\rho_{23}}\frac{1}{kH_1} + \frac{\sigma_3 B^2}{\Delta\rho_{12} + \epsilon^2\Delta\rho_{23}}\frac{\epsilon^2}{kH_3}\right)\left(-\frac{1}{2} + \frac{m}{k^2R^2 - m^2}\right) \tag{A 2}$$

We have used the shallow limit formulas to create the dashed lines in figure 10 that clearly converge towards the general theory for the cylindrical equivalent cells of Tucs *et al.* (2018*a*).

A.2. *Deep-shallow-deep limit*

The theoretical formulas take particularly simple forms in the limit of shallow electrolyte layer and deep top and bottom layers. Using

$$\overline{\rho}_{12} \approx \rho_1 + \frac{\rho_2}{kH_2} \quad , \quad \overline{\rho}_{23} \approx \rho_3 + \frac{\rho_2}{kH_2} \tag{A 3}$$

we find that $\omega_\pm^2$ for the slow and fast branches reach the following leading order limits

$$\omega_-^2 \approx \frac{\Delta\rho_{12}\Delta\rho_{23}\, gk}{\rho_2\,\Delta\rho_{13}}\, kH_2 \quad , \quad \omega_+^2 \approx \frac{\Delta\rho_{13}\, gk}{\rho_1 + \rho_3} = \omega_{13}^2 \tag{A 4}$$

Here we denote $\Delta\rho_{13} = \rho_3 - \rho_1$. The slow wave branch is gradually approaching zero as $kH_2 \rightarrow 0$, whereas the rapid branch tends towards the dispersion relation of the two-layer fluid system with liquid 1 above liquid 3. Along with these branches, we find the amplitude ratios as

$$\epsilon_- \approx -\frac{\Delta\rho_{12}}{\Delta\rho_{23}} \quad , \quad \epsilon_+ \approx 1 + kH_2\left(\frac{\rho_1\Delta\rho_{23}}{\rho_2\Delta\rho_{13}} - \frac{\rho_3\Delta\rho_{12}}{\rho_2\Delta\rho_{13}}\right) \tag{A 5}$$

As in Horstmann *et al.* (2018), the amplitude ratio of the fast waves $\epsilon_+ \approx 1$, which means that upper and lower interfaces are similarly deformed. We need the $O(kH_2)$ correction in ϵ_+ to compute the leading order dissipation-less growth rate that we find as

$$\lambda_{v,-} \approx \frac{m}{\kappa_{mn}^2 - m^2}\frac{JB_z}{\sqrt{g}}\frac{1}{\sqrt{H_2}}\frac{\Delta\rho_{12} - \Delta\rho_{23}}{2\sqrt{\rho_2\Delta\rho_{12}\Delta\rho_{23}\Delta\rho_{13}}} \tag{A 6a}$$

$$\lambda_{v,+} \approx \frac{m}{\kappa_{mn}^2 - m^2}\frac{JB_z}{\sqrt{g}}\sqrt{k}\sqrt{\frac{\Delta\rho_{13}}{\rho_1 + \rho_3}}\,\frac{\rho_1\Delta\rho_{23} - \rho_3\Delta\rho_{12}}{\rho_2\Delta\rho_{13}^2} \tag{A 6b}$$

These formulas show more clearly that the dissipation-less growth rate can be very small, that MPR-instability may be very weak in LMBs. In this deep-shallow-deep limit, slow waves are always very weakly destabilised near $\Delta\rho_{12}/\Delta\rho_{23} = 1$. Fast modes are weakly destabilised

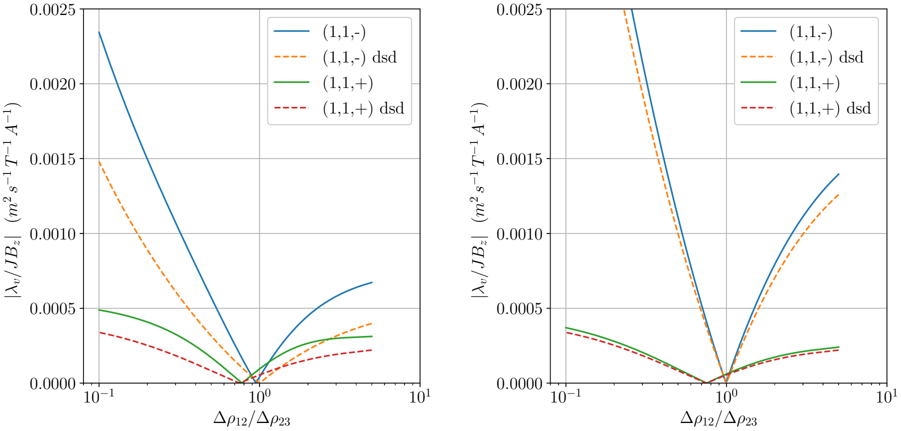

(a) $(R, H_1, H_2, H_3) = (5, 4.5, 1, 4.5)$ cm (b) $(R, H_1, H_2, H_3) = (5, 7, 0.1, 7)$ cm

Figure 13: Comparison of deep-shallow-deep limit formulas for the dissipation-less relative growth rate λ_v/JB_z to the general theory and for two different geometries, (a) the cell of Horstmann *et al.* (2018), (b) a cell with taller metal zones and a thinner electrolyte layer. Material properties are as in (3.11).

near $\Delta\rho_{12}/\Delta\rho_{23} = \rho_1/\rho_3$. Far away from these values, we see that $\lambda_{v,+}/\lambda_{v,-} \sim \sqrt{kH_2} \ll 1$. This suggests that slow - waves will most often be the more unstable ones, except in the vicinity of $\Delta\rho_{12}/\Delta\rho_{23} = 1$.

In figure 13, we compare the general theory to the deep-shallow-deep limit. We show the relative dissipation-less growth rate $|\lambda_v|/JB_z$ for the cell of Horstmann *et al.* (2018) with variable $\rho_1 \in [500, 2950]$ kg m^{-3} and $(\rho_2, \rho_3) = (3000, 3500)$ kg m^{-3}. In panel (a), we see that in the original set-up with fluid layers of height $(R, H_1, H_2, H_3) = (5, 4.5, 1, 4.5)$ cm MPR-instability is not well modeled by this deep-shallow-deep limit. For taller top and bottom layers and with a thinner electrolyte, for example $(R, H_1, H_2, H_3) = (5, 7, 0.1, 7)$ cm, the deep-shallow-deep limit is well adapted, see panel (b).

REFERENCES

Ashour, R., Kelley, D. H., Salas, A., Starace, M., Weber, N. & Weier, T. 2018 Competing forces in liquid metal electrodes and batteries. *J. Power Sources* **378**, 301–310.

Bojarevics, V. 1998 Nonlinear waves with electromagnetic interaction in aluminum electrolysis cells. *Progress in astronautics and aeronautics* **182**, 833–848.

Bojarevics, V., Freibergs, J. A., Shilova, E. I. & Shcherbinin, E. V. 1989 *Electrically Induced Vortical Flows*. Kluwer Academic Publishers.

Bojarevics, V. & Romerio, M.V. 1994 Long waves instability of liquid metal-electrolyte interface in aluminium electrolysis cells: a generalization of sele's criterion. *European Journal of Mechanics B/ Fluids* **13**, 33–33.

Bojarevics, V. & Tucs, A. 2017 MHD of large scale liquid metal batteries. In *Light Metals 2017*, pp. 687–692. Springer.

Bradwell, D. J., Kim, H., Sirk, A. H. C. & Sadoway, D. R. 2012 Magnesium–antimony liquid metal battery for stationary energy storage. *Journal of the American Chemical Society* **134** (4), 1895–1897.

Cappanera, L., Guermond, J.-L., Herreman, W. & Nore, C. 2018 Momentum-based approximation of incompressible multiphase fluid flows. *International Journal for Numerical Methods in Fluids* **86** (8), 541–563.

Case, K.M. & Parkinson, W.C. 1957 Damping of surface waves in an incompressible liquid. *Journal of Fluid Mechanics* **2** (02), 172–184.

Davidson, P.A. & Lindsay, R.I. 1998 Stability of interfacial waves in aluminium reduction cells. *Journal of Fluid Mechanics* **362**, 273–295.

Gerbeau, J.-F., Le Bris, C. & Lelièvre, T. 2006 *Mathematical methods for the magnetohydrodynamics of liquid metals*. Clarendon Press.

Guermond, J.-L., Laguerre, R., Léorat, J. & Nore, C. 2007 An interior penalty Galerkin method for the MHD equations in heterogeneous domains. *J. Comput. Phys.* **221** (1), 349–369.

Guermond, J.-L., Laguerre, R., Léorat, J. & Nore, C. 2009 Nonlinear magnetohydrodynamics in axisymmetric heterogeneous domains using a Fourier/finite element technique and an interior penalty method. *J. Comput. Phys.* **228** (8), 2739–2757.

Herreman, W., Nore, C., Cappanera, L. & Guermond, J.-L. 2021 Efficient mixing by swirling electrovortex flows in liquid metal batteries. *Journal of Fluid Mechanics* **915**, A17.

Herreman, W., Nore, C., Guermond, J.-L., Cappanera, L., Weber, N. & Horstmann, G.M. 2019 Perturbation theory for metal pad roll instability in cylindrical reduction cells. *Journal of Fluid Mechanics* **878**, 598–546.

Horstmann, G. M., Weber, N. & Weier, T. 2018 Coupling and stability of interfacial waves in liquid metal batteries. *Journal of Fluid Mechanics* **845**, 1–35.

Horstmann, G. M. & Wylega, M.and Weier, T. 2019 Measurement of interfacial wave dynamics in orbitally shaken cylindrical containers using ultrasound pulse-echo techniques. *Experiments in Fluids* **60** (4), 1–17.

Landau, L. D. & Lifshitz, E. M. 1987 *Fluid Mechanics*. Pergamon Press.

Lukyanov, A., El, G. & Molokov, S. 2001 Instability of MHD-modified interfacial gravity waves revisited. *Physics Letters A* **290** (3), 165–172.

Molokov, S 2018 The nature of interfacial instabilities in liquid metal batteries in a vertical magnetic field. *Europhysics Letters* **121** (4), 44001.

Nore, C., Cappanera, L., Guermond, J.-L., Weier, T. & Herreman, W. 2021 Feasibility of metal pad roll instability experiments at room temperature. *Physical Review Letters* **126** (18), 184501.

Nore, C., Quiroz, D. Castanon, Cappanera, L. & Guermond, J.-L. 2016 Direct numerical simulation of the axial dipolar dynamo in the Von Kármán sodium experiment. *EPL (Europhysics Letters)* **114** (6), 65002.

Pedchenko, A., Molokov, S. & Bardet, B. 2016 The effect of "wave breakers" on the magnetohydrodynamic instability in aluminum reduction cells. *Metallurgical and Materials Transactions B* pp. 1–5.

Pedchenko, A., Molokov, S., Priede, J., Lukyanov, A. & Thomas, P.J. 2009 Experimental model of the interfacial instability in aluminium reduction cells. *Europhysics Letters* **88** (2), 24001.

Sele, T. 1977 Instabilities of the metal surface in electrolytic alumina reduction cells. *Metallurgical and Materials Transactions B* **8** (4), 613–618.

Steiner, G. 2009 Simulation numérique de phénomènes MHD: application à l'électrolyse de l'aluminium. PhD thesis, École Polytechnique Fédérale de Lausanne.

Sun, H., Zikanov, O. & Ziegler, D.P. 2004 Non-linear two-dimensional model of melt flows and interface instability in aluminum reduction cells. *Fluid Dynamics Research* **35** (4), 255–274.

Tucs, A., Bojarevics, V. & Pericleous, K. 2018*a* Magneto-hydrodynamic stability of a liquid metal battery in discharge. *Europhys. Lett.* **124**, 24001.

Tucs, A., Bojarevics, V. & Pericleous, K. 2018*b* Magnetohydrodynamic stability of large scale liquid metal batteries. *Journal of Fluid Mechanics* **852**, 453–483.

Viola, F. & Gallaire, F. 2018 Theoretical framework to analyze the combined effect of surface tension and viscosity on the damping rate of sloshing waves. *Physical Review Fluids* **3**, 094801.

Wang, K., Jiang, K., Chung, B., Ouchi, T., Burke, P. J., Boysen, D. A., Bradwell, D. J., Kim, H., Muecke, U. & Sadoway, D. R. 2014 Lithium-antimony-lead liquid metal battery for grid-level energy storage. *Nature* **514** (7522), 348–350.

Weber, N., Beckstein, P., Galindo, V., Herreman, W., Nore, C., Stefani, F. & Weier, T. 2017*a* Metal pad roll instability in liquid metal batteries. *Magnetohydrodynamics* **53** (1), 129–140.

Weber, N., Beckstein, P., Herreman, W., Horstmann, G.M., Nore, C., Stefani, F. & Weier, T. 2017*b* Sloshing instability and electrolyte layer rupture in liquid metal batteries. *Physics of Fluids* **29** (5), 054101.

Xiang, L. & Zikanov, O. 2019 Numerical simulation of rolling pad instability in cuboid liquid metal batteries. *Physics of Fluids* **31** (12), 124104.

Zikanov, O. 2015 Metal pad instabilities in liquid metal batteries. *Physical Review E* **92** (6), 063021.

Zikanov, O. 2018 Shallow water modeling of rolling pad instability in liquid metal batteries. *Theoretical and Computational Fluid Dynamics* **32** (3), 325–347.

Zikanov, O., Sun, H. & Ziegler, D.P. 2004 Shallow water model of flows in Hall-Héroult cells. *Light Metals* pp. 445–452.

Zikanov, O., Thess, A., Davidson, P.A. & Ziegler, D.P. 2000 A new approach to numerical simulation of melt flows and interface instability in hall-heroult cells. *Metallurgical and Materials Transactions B* **31** (6), 1541–1550.